

Special Section:

Science and Exploration of the Moon, Near-Earth Asteroids, and the Moons of Mars

Key Points:

- Particle size is an important variable affecting the position of the Christiansen feature under a simulated lunar environment
- Particle size variation is within the detectable limits of the Diviner Lunar Radiometer Experiment
- Future mid-infrared missions will benefit from a simulated lunar environment spectral library

Supporting Information:

- Supporting Information S1

Correspondence to:K. A. Shirley,
katherine.shirley@stonybrook.edu**Citation:**Shirley, K. A., & Glotch, T. D. (2019). Particle size effects on mid-infrared spectra of lunar analog minerals in a simulated lunar environment. *Journal of Geophysical Research: Planets*, 124, 970–988. <https://doi.org/10.1029/2018JE005533>

Received 12 JAN 2018

Accepted 15 JAN 2019

Accepted article online 21 JAN 2019

Published online 17 APR 2019

Particle Size Effects on Mid-Infrared Spectra of Lunar Analog Minerals in a Simulated Lunar Environment

K. A. Shirley¹  and T. D. Glotch¹ ¹Department of Geosciences, Stony Brook University, Stony Brook, NY, USA

Abstract Mid-infrared spectroscopic analysis of the Moon and other airless bodies requires a full accounting of spectral variation due to the unique thermal environment in airless body regoliths and the substantial differences between spectra acquired under airless body conditions and those measured in an ambient environment on Earth. Because there exists a thermal gradient within the upper hundreds of microns of lunar regolith, the data acquired by the Diviner Lunar Radiometer Experiment are not isothermal with wavelength. While this complication has been previously identified, its effect on other known variables that contribute to spectral variation, such as particle size and porosity, have yet to be well characterized in the laboratory. Here we examine the effect of particle size on mid-infrared spectra of silicates common to the Moon measured within a simulated lunar environment chamber. Under simulated lunar conditions, decreasing particle size is shown to enhance the spectral contrast of the Reststrahlen bands and transparency features, as well as shift the location of the Christiansen feature to longer wavelengths. This study shows that these variations are detectable at Diviner spectral resolution and emphasizes the need for simulated environment laboratory data sets, as well as hyperspectral mid-infrared instruments on future missions to airless bodies.

Plain Language Summary When trying to determine the composition of a planetary surface, it is important to have a basis for comparison. Currently, infrared data acquired from missions to airless bodies, like the Moon and asteroids, are mostly compared to data measured under ambient terrestrial conditions, and the difference in measurement environment complicates analysis. In this work, we measure minerals of varying particle size in the laboratory under a simulated lunar environment to understand how this variable affects the data, and whether we can detect the variations with the Lunar Reconnaissance Orbiter Diviner Lunar Radiometer Experiment. Acquiring infrared data under simulated lunar environment conditions will improve our interpretation of data not only from the Moon but also from other airless planetary bodies such as Mercury and asteroids.

1. Introduction

Mid-infrared (MIR; 6–25 μm) spectroscopy is a useful tool for analyzing the surface composition of planetary surfaces. The MIR is especially important for identifying silicates, major constituents of rocky planetary bodies, that exhibit strong fundamental vibration features within this wavelength range (e.g., Lyon, 1964). The current, and only, lunar MIR instrument is the Diviner Lunar Radiometer Experiment (Diviner) on the Lunar Reconnaissance Orbiter. Diviner measures radiance from 0.3 to 400 μm , which can be converted to emissivity to inform us about the bulk silicate mineralogy across the surface of the Moon (Greenhagen et al., 2010; Paige, Foote, et al., 2010), as well as the thermophysical properties of the lunar regolith (e.g., Bandfield et al., 2011, 2015; Elder et al., 2017; Paige, Siegler, et al., 2010; Siegler et al., 2015, 2016; Vasavada et al., 2012). Diviner has contributed to a better understanding of lunar geology, such as highly silicic features (e.g., Glotch et al., 2010), crater peak compositions (e.g., Song et al., 2013), and lunar swirls (e.g., Glotch et al., 2015) and shown how well Diviner data can complement visible to near-infrared data, such as the assessment of lunar crystalline plagioclase (e.g., Donaldson Hanna et al., 2014), examination of volcanics (e.g., Bennett et al., 2016), and quantification of olivine content (e.g., Arnold et al., 2016).

There are numerous difficulties associated with using MIR spectroscopy to analyze remote sensing data from an airless body like the Moon, because most MIR emissivity data to which we compare our remote sensing data have been collected under terrestrial conditions. Early work (e.g., Conel, 1969; Henderson & Jakosky, 1997; Logan & Hunt, 1970; Nash et al., 1993; Salisbury et al., 1995) has shown the importance of environmental conditions (e.g., pressure, temperature of the surrounding medium, and illumination conditions)

Table 1
Mineral Sample Chemistry Averaged From Five Grains and Standard Deviation

Mineral	SiO ₂	MgO	Al ₂ O ₃	Na ₂ O	K ₂ O	CaO	MnO	FeO	TiO ₂	Cr ₂ O ₃	P ₂ O ₅	NiO
Quartz	100.692 (0.331)	0 (0.004)	0.153 (0.155)	0.014 (0.006)	0 (0.003)	0.006 (0.011)	0 (0.005)	0 (0.009)	0.002 (0.009)	0 (0.008)	0 (0.010)	0 (0.022)
Anorthite	43.482 (0.159)	0.086 (0.024)	35.668 (0.198)	0.534 (0.048)	0.005 (0.007)	19.816 (0.227)	0 (0.017)	0.456 (0.027)	0.005 (0.009)	0 (0.009)	0.010 (0.013)	0.001 (0.013)
Labradorite	55.870 (0.481)	0.004 (0.007)	28.438 (0.410)	5.655 (0.068)	0.503 (0.196)	10.462 (0.406)	0.011 (0.009)	0.156 (0.068)	0.032 (0.054)	0 (0.006)	0.028 (0.017)	0.003 (0.020)
Albite	62.563 (0.125)	0.003 (0.006)	24.288 (0.045)	8.872 (0.057)	0.375 (0.051)	5.375 (0.081)	0.008 (0.010)	0.046 (0.014)	0.001 (0.008)	0 (0.004)	0 (0.008)	0 (0.009)
Augite	52.688 (0.160)	11.957 (0.073)	0.703 (0.154)	0.493 (0.064)	0 (0.004)	25.179 (0.223)	0.278 (0.021)	9.853 (0.136)	0.017 (0.004)	0.022 (0.015)	0.011 (0.019)	0.004 (0.019)
Diopside	54.382 (0.190)	15.881 (0.165)	0.229 (0.094)	0.097 (0.008)	60.6 ppm (0.005)	26.184 (0.218)	0.593 (0.055)	3.548 (0.180)	0.004 (0.003)	0 (0.005)	0.022 (0.010)	0.013 (0.017)
Enstatite	52.057 (0.166)	24.370 (0.309)	3.749 (0.446)	0.006 (0.006)	0.002 (0.011)	0.377 (0.077)	0.318 (0.031)	18.254 (0.391)	0.087 (0.021)	0.088 (0.017)	0.008 (0.007)	0.024 (0.014)
Forsterite	40.939 (0.292)	49.785 (1.281)	0.024 (0.010)	0.032 (0.005)	0 (0.004)	0.087 (0.011)	0.141 (0.025)	10.121 (1.590)	0 (0.003)	0.016 (0.011)	0.002 (0.012)	0.365 (0.015)
Ilmenite	0 (0.007) (0.165)	3.679 (0.010)	0.036 (0.056)	0.036 (0.056)	0.007 (0.006)	0.031 (0.013)	0.481 (0.037)	43.571 (0.508)	51.434 (0.497)	0.005 (0.009)	0.038 (0.016)	0.011 (0.010)

when measuring MIR spectra and how features can shift in both position and spectral contrast due to variations in those conditions. Recent studies (Donaldson Hanna, Thomas, et al., 2012; Donaldson Hanna, Wyatt, et al., 2012; Donaldson Hanna et al., 2014, 2017; Lucey et al., 2017) have sought to produce MIR spectra that more closely match those measured by Diviner to optimize our ability to interpret lunar spectra.

The purpose of this work is to further explore the effects of environment conditions on spectra by examining the role of particle size, a variable known to cause variations on spectral contrast under ambient conditions (Lyon, 1964, Mustard & Hays, 1997; Cooper et al., 2002), on MIR spectra of minerals; to compare these effects under simulated lunar conditions and in Earth-like (ambient) conditions; and to create a spectral library for minerals under simulated lunar conditions to enhance our ability to interpret data from the surface of airless bodies.

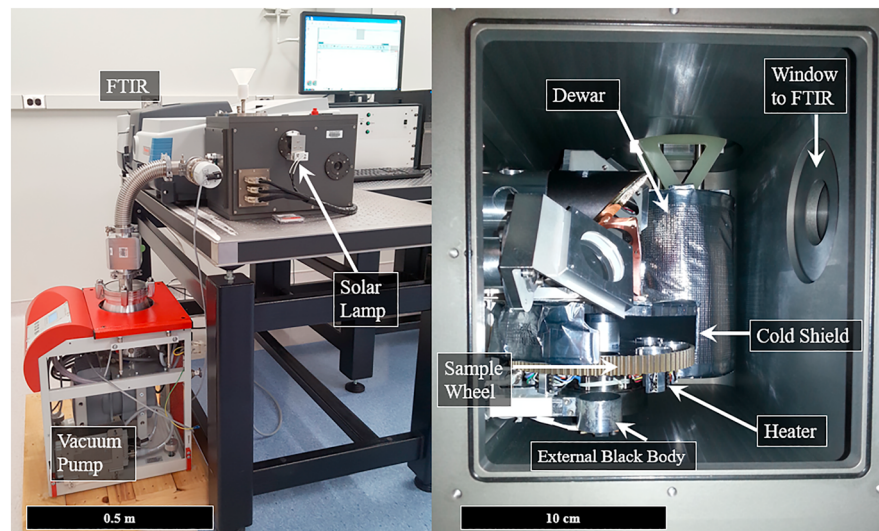


Figure 1. Laboratory setup showing the major pieces of equipment (a) including FTIR spectrometer, vacuum pump, and PARSEC as well as a view of (b) the interior of PARSEC. PARSEC = Planetary and Asteroid Regolith Spectroscopy Environmental Chamber.

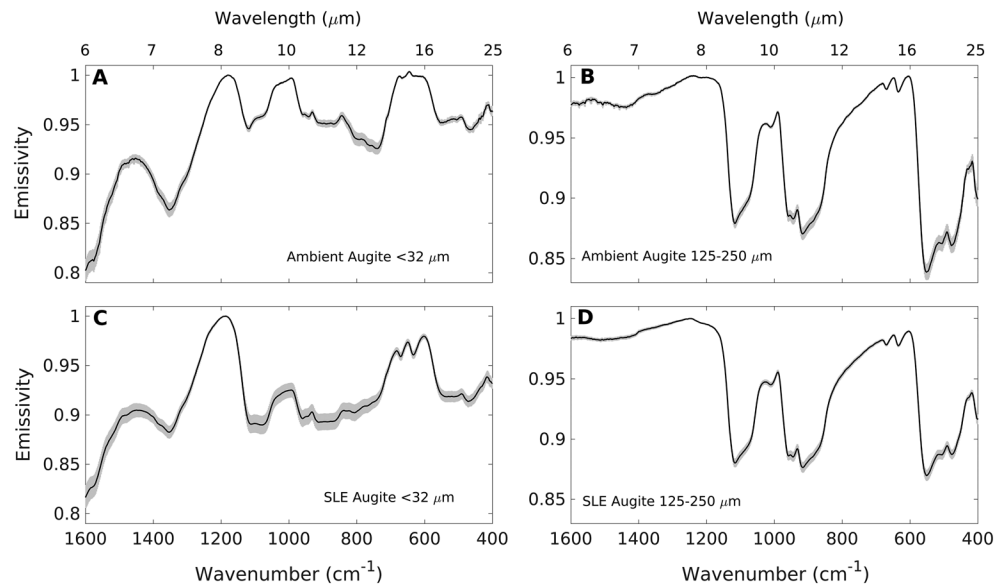


Figure 2. Augite spectra (black) with the emissivity error per wavelength (gray) as produced from 11 repeated measurements of the same sample under the same preparation and measurement technique for both <32 and $125\text{--}250\ \mu\text{m}$ under ambient (a and b) and SLE (c and d) conditions. Absolute error in emissivity is $<3\%$ for the range of interest $1600\text{--}400\ \text{cm}^{-1}$. SLE = simulated lunar environment.

2. Background

2.1. The Lunar Regolith

Silicates are the most common minerals in our solar system and have been identified on the Moon from returned samples and from orbit. Analyses of lunar samples and remote sensing data have shown the lunar surface to be dominated by plagioclase feldspar, pyroxenes, agglutinitic glasses of similar compositions, and, in some mare basalts and central peaks, olivine (e.g., Papike et al., 1982, 1991, 1998; Smith & Steele, 1976; Wieczorek et al., 2006). The feldspar is generally $\text{An}_{94\text{--}98}$ for ferroan anorthosites and $\text{An}_{65\text{--}98}$ in the Alkali-suite (e.g., Taylor, 2009; Vaniman & Papike, 1980). The pyroxenes are broadly quadrilateral in composition and abundant in lunar basalts (e.g., Papike et al., 1976; Papike & Vaniman, 1978), and olivine is generally $\text{Fo}_{30\text{--}80}$ (e.g., Wieczorek et al., 2006). Additionally, the oxide ilmenite is abundant in some mare basalts (McKay & Williams, 1979; Rutherford et al., 1980) and spinel has been shown to be

an important phase based on both laboratory and remote sensing studies (Jackson et al., 2014; Marriner et al., 2014, 2015; Nekvasil et al., 2015; Pieters et al., 2011, 2014; Williams et al., 2016). Analyses of sieved bulk Apollo soils have shown an average particle size of $\sim 60\ \mu\text{m}$, with a median range between 40 and $130\ \mu\text{m}$ with a depth dependence where material at the top of the regolith column has a smaller average particle size (Carrier, 1973; Heiken et al., 1973; King et al., 1971, 1972a, 1972b; McKay et al., 1972, 1974).

From a remote sensing standpoint, Pieters et al. (1993) have shown that the smallest size fraction ($<25\ \mu\text{m}$) is spectrally dominant, at least in the visible to near-infrared range, and early studies by Logan et al. (1973) suggest similar small particle size ($<74\ \mu\text{m}$) in the MIR for the Moon. Bandfield et al. (2011) demonstrated that little of the upper few centimeters of regolith across the lunar surface is rocky; however, young fresh craters tend to have regolith particle size heterogeneity detectable by Diviner (Bandfield et al., 2011, 2017), and future hyperspectral or surface missions could benefit from a spectral library of varying particle size as exist for studies of the Earth and Mars.

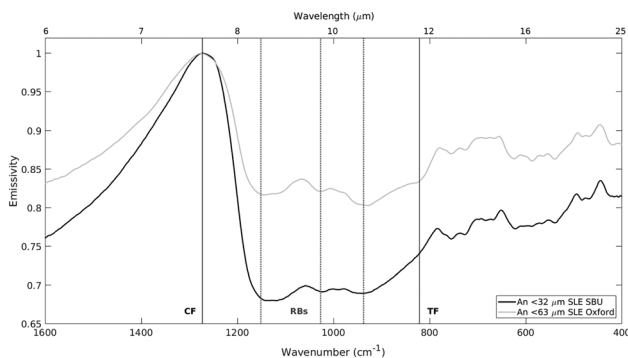


Figure 3. Comparison of anorthite spectra measured at PARSEC (black) and at SLEC (gray) under SLE conditions. Both environmental chambers produce similar spectral feature positions, with spectral contrast variation due to the sample being heated to $120\ ^\circ\text{C}$ at SLEC and $80\ ^\circ\text{C}$ at PARSEC. PARSEC = Planetary and Asteroid Regolith Spectroscopy Environmental Chamber; SLE = simulated lunar environment.

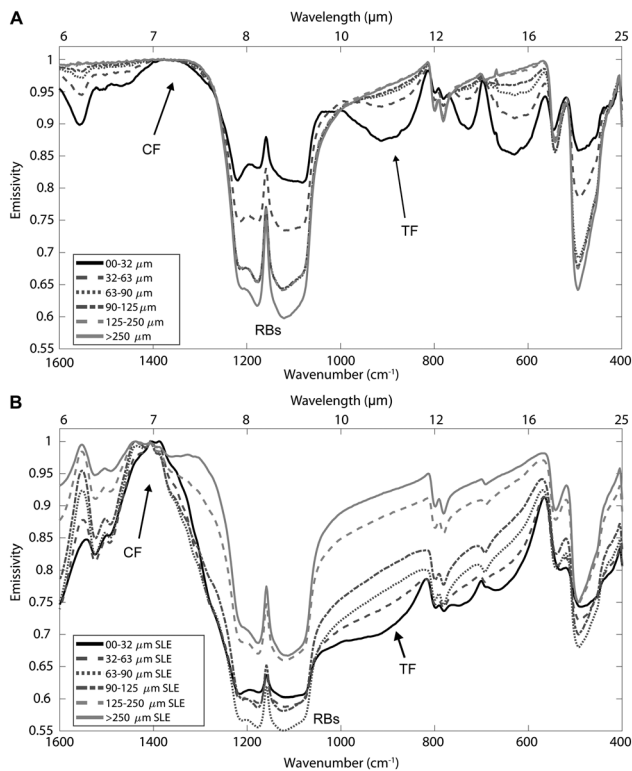


Figure 4. Mid-infrared emissivity spectra of quartz with particle size variation measured under ambient conditions (a) and simulated lunar environment conditions (b). Christiansen feature (CF), Reststrahlen bands (RBs), and transparency features (TF) are labeled.

2.2. MIR Spectroscopy Features

Diagnostic features of mid-infrared spectra are the Christiansen feature (CF), Reststrahlen bands (RBs), and transparency features (TFs). The CF is an emissivity maximum that occurs near the Christiansen frequency where the real refractive index of the material is approximately equal to the refractive index of the medium ($n = 1$ for air or vacuum), and where the imaginary refractive index, k , is small. Its position is indicative of silica polymerization where highly polymerized (framework) silicates have a CF at shorter wavelengths or higher wave numbers (Conel, 1969; Logan et al., 1973). The RBs are caused by the stretching and bending of bonds between silicon, oxygen, and various cations and are therefore important in identifying feldspars, pyroxenes, and olivine among other minerals (e.g., Conel, 1969; Donaldson Hanna, Wyatt, et al., 2012; Hamilton, 2000; Lyon, 1964). TFs are emissivity minima caused by volume scattering and become more pronounced as particle size decreases (e.g., Cooper et al., 2002).

Previous studies (e.g., Hamilton, 2000; Lyon, 1964; Mustard & Hays, 1997; Salisbury & Eastes, 1985; Salisbury et al., 1987; Salisbury & Wald, 1992; Vincent & Hunt, 1968) have shown the importance of particle size on both the RBs, which lose spectral contrast, and TFs, which gain spectral contrast, as particle size decreases when measured under ambient conditions. Studies performed under lunar environment conditions (e.g., Conel, 1969; Donaldson Hanna, Thomas, et al., 2012; Henderson & Jakosky, 1994; Salisbury et al., 1970) have shown shifts in the CF and spectral contrast from spectra measured under ambient conditions; however, this is the first analysis of the effect of particle size on MIR emissivity spectra of a variety of silicates measured under simulated lunar environment conditions.

2.3. Lunar Environment Conditions

On Earth and Mars, heat transfer in the regolith is primarily accomplished through convection by air molecules in regolith pore spaces. On the Moon and other airless bodies in the solar system, there is no interstitial gas to facilitate heat transfer between grains of regolith, so heat is transferred through the less-efficient processes of radiation and conduction between grain boundaries (Henderson & Jakosky, 1994; Logan & Hunt, 1970). As a result, while illuminated and heated by solar irradiation, the particles at the uppermost surface quickly lose that heat to space, but, moving deeper within the top several hundred microns of lunar regolith, the temperature of the particles increases. Thus, we observe a thermal gradient so that both warm and cold temperatures from different depths contribute to the measured spectral thermal emission. Henderson and Jakosky (1997) modeled the thermal gradient expected on the Moon and determined it to be up to 40 K/100 μm . Effects of this gradient on emission spectra have been modeled and measured in the lab in several additional studies (e.g., Donaldson Hanna, Wyatt, et al., 2012; Henderson & Jakosky, 1994, 1997; Logan & Hunt, 1970; Millán et al., 2011) showing shifts in the CF and overall spectral contrast when compared to samples measured under terrestrial ambient conditions.

2.4. The Diviner Lunar Radiometer

The Diviner Lunar Radiometer Experiment has enabled the first systematic high spatial resolution compositional measurements of the Moon at MIR wavelengths. Diviner was launched in 2009 on the Lunar Reconnaissance Orbiter and has acquired near continuous radiometric measurements of the lunar surface since orbit insertion. Diviner is a nine-channel push-broom radiometer containing 21 detectors per channel where each detector has 240- by 480- μm pixels with a ground resolution of ~ 160 m (cross track) by 320 m (along track) from the 50-km circular orbit (Paige, Foote, et al., 2010). Channels 1 and 2 are dedicated to broadband visible albedo measurements. Channels 3–5 are narrow band channels dedicated to compositional analysis and are centered at $7.80 \pm 0.25 \mu\text{m}$, $8.25 \pm 0.15 \mu\text{m}$, and $8.55 \pm 0.17 \mu\text{m}$, respectively.

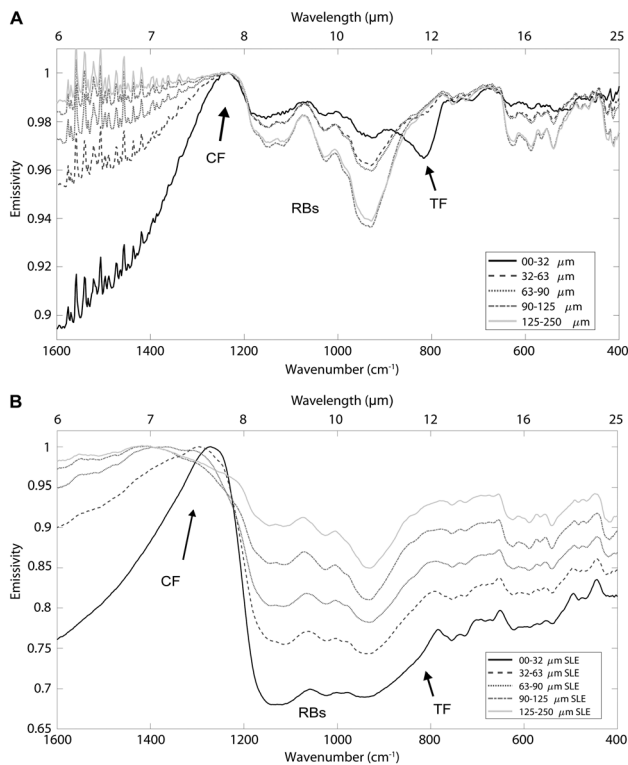


Figure 5. Mid-infrared emissivity spectra of anorthite with variation in particle size measured under ambient conditions (a) and simulated lunar environment conditions (b). Christiansen feature (CF), Reststrahlen bands (RBs), and transparency features (TF) are labeled. The features between 1300 and 1600 cm^{-1} in (a) are due to water vapor in the chamber atmosphere.

Channels 6–9 are broadband thermal channels used for temperature measurements over a range of lunar surface conditions, which cover 13–23 μm , 25–41 μm , 50–100 μm , and 100–400 μm , respectively. Channels 3–5, centered near the CF have been used in several studies to characterize the bulk composition and optical maturity of the lunar surface (e.g., Arnold et al., 2016; Ashley et al., 2016; Boyce et al., 2018; Glotch et al., 2010, 2011, 2015; Greenhagen et al., 2010; Jolliff et al., 2011; Lucey et al., 2017; Song et al., 2013).

Parabolic fitting of Channels 3–5 has been used to estimate the CF position and spectral shape from Diviner data, providing an indicator of lunar surface lithologies (Allen et al., 2012; Donaldson Hanna, Thomas, et al., 2012; Donaldson Hanna, Wyatt, et al., 2012; Donaldson Hanna et al., 2014, 2017; Glotch et al., 2010, 2011, 2015; Greenhagen et al., 2010; Greenhagen & Paige, 2006; Paige, Foote, et al., 2010; Song et al., 2013). Additionally, a concavity index of Channels 3–5 (Glotch et al., 2010) is used when the CF position falls outside of the three channels, as in when Diviner only registers a side of the parabola without the maximum. These extreme CF positions occur in highly silicic regions where CF position is short of 7.8 μm , and in olivine-rich regions where the CF position falls longward of 8.6 μm (Arnold et al., 2016; Ashley et al., 2016; Boyce et al., 2018; Glotch et al., 2010, 2011).

3. Methods

3.1. Sample Preparation

Samples used in this study include: quartz, anorthite (An_{95}), labradorite (An_{49}), albite (An_{24}), augite ($\text{Wo}_{50}\text{En}_{34}\text{Fs}_{16}$), diopside ($\text{Wo}_{51}\text{En}_{43}\text{Fs}_6$), enstatite ($\text{Wo}_1\text{En}_{70}\text{Fs}_{29}$), forsterite (Fo_{88}), and ilmenite to investigate a range of silicates and ilmenite relevant to the Moon. All samples are natural terrestrial samples chosen to represent a range of silicate compositions within each mineral group. Samples were ground to sand sized particles ($\sim 250 \mu\text{m}$) using an agate mortar and pestle, hand picked, and assessed for quality using an optical microscope and electron-probe microanalysis (EPMA). EPMA analyses were performed on a JEOL JXA-8200 electron microprobe equipped with five wavelength-dispersive spectrometers, and a JEOL (e2v/Gresham) silicon-drift energy-dispersive spectrometer. Analyses are acquired using the Probe for EPMA analysis software, and X-ray correction is performed using the CITZAF correction software (Armstrong, 1995). Typical operating conditions are 15 KV accelerating potential and 25 nA probe current. Standards used in the facility range from pure elements and oxides to simple or complex silicates and glasses recognized throughout the analytical community. One or two measurements per grain on five to ten grains greater than 125 μm per sample were analyzed and averaged together to get the mineral chemistry in Table 1.

The samples were hand ground and dry sieved to <32, 32–63, 63–90, 90–125, and 125–250 μm size fractions using an Advantech Sonic Sifter. These size fractions were chosen to cover the range of particle sizes in Apollo soils (Carrier, 1973; Heiken et al., 1973; King et al., 1971, 1972a, 1972b; McKay et al., 1972, 1974). Advantech guarantees precision in dry sieving due to the tapping of the sonic pulses meant to disrupt aggregation of extremely fine particles (<45 μm) which can adhere to larger particles (*advantechmfg.com*). While standard dry sieving may result in clinging fines, these appear minimal in the separates based on microscope analysis, and there is little evidence that they are significant based on the ambient MIR spectra, which have trends due to particle size, consistent with those noted in previous works (e.g., Cooper et al., 2002; Mustard & Hays, 1997).

Samples were poured into 2.3-cm diameter aluminum sample cups to maintain a rough surface similar to what would be expected for a natural regolith surface (i.e., not a smoothed or flattened surface) to $\sim 75\%$ cup capacity, and then loaded into the Planetary and Asteroid Regolith Spectroscopy Environmental Chamber (PARSEC) at the Center for Planetary Exploration (CPEX) at Stony Brook University for all

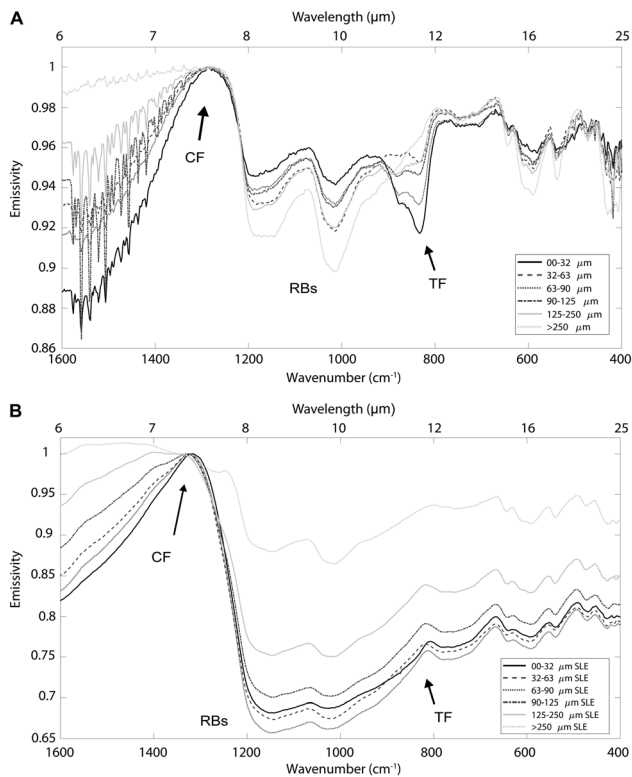


Figure 6. Mid-infrared emissivity spectra of albite measured under ambient conditions (a) and simulated lunar environment conditions (b) with particle size variation. Christiansen feature (CF), Reststrahlen bands (RBs), and transparency features (TF) are labeled. The features between 1300 and 1600 cm^{-1} in (a) are due to water vapor in the chamber atmosphere.

MIR spectroscopic measurements, see Figure 1 for laboratory setup. Sample cup volume was evaluated and determined to produce similar spectra and gradients when between 75% full and 100% full, thus 75% full was chosen to accommodate limited sample material (Shirley, 2018). While surface roughness is known to create variations in spectra (Donaldson Hanna et al., 2017), the repeatability of this sample preparation technique has been evaluated by making 11 measurements, removing the sample from the cup, and repouring between each measurement using augite of <32- and 125- to 250- μm size fractions to produce spectra within <3% emissivity variation for both size fractions and measurement conditions within the 1600–400 cm^{-1} spectral range (Figure 2).

3.2. Data Acquisition

PARSEC was built at the University of Oxford and modeled after their Simulated Lunar Environment Chamber (Thomas et al., 2012) to measure samples under environmental conditions of airless planetary bodies (e.g., Moon and asteroids). PARSEC contains a sample wheel on which sit six sample cups and a calibration target that is ridged and coated in Nextel black, as well as a black body under the wheel also painted with Nextel black, all of which are capable of individual heating and can be rotated into measurement position via the external control box. Temperature of the samples and black body targets is controlled by two Eurotherm Mini8 Loop Controllers and managed with the Eurotherm iTools interface. Samples are illuminated at 55° incidence by a quartz halogen lamp connected to a tunable Bentham 610 power source for adjustable wattage. The PARSEC cold shield surrounding the sample wheel is actively cooled via input of liquid nitrogen into an internal dewar (Figure 1) to reach temperatures of <150 K. Pressure is controlled by a Pfeiffer HiCube turbo vacuum pump to reach $<10^{-6}$ mbar.

PARSEC is connected to a Nicolet 6700 Fourier Transform Infrared (FTIR) spectrometer equipped with a potassium bromide (KBr) beamsplitter and a deuterated L-alanine doped triglycine sulfate (DLATGS) detector with a KBr window, integrating 256 scans for a ~10-min measurement of thermal emission across 2,200–400 cm^{-1} (4.5–25 μm) with a resolution of 2 cm^{-1} at 0° emission angle for each sample, black body, or calibration target. The spectrometer is actively purged with air scrubbed of CO_2 and water vapor and sealed to the exterior of PARSEC. The FTIR spectrometer settings are controlled and spectra acquired via Thermo Fisher Scientific OMNIC 9 software.

Samples were measured under terrestrial ambient conditions (ambient), and then under simulated lunar environment (SLE) conditions. Ambient is defined as pressure at 1,000 mbar, in regular air, chamber temperature at $\sim 300 \pm 1$ K, sample temperature at 350 ± 0.5 K, with no illumination, similar to ambient conditions of other spectral libraries, such as at ASU (Christensen et al., 2000). SLE conditions are achieved by pumping the chamber down to a pressure of $<10^{-5}$ mbar, heating the samples from below to 350 ± 0.5 K, heating from above via quartz halogen lamp connected to a tunable power source, and cooling the chamber to <150 K with variation within ± 2 K during a measurement, as measured at the cold shield. Samples are allowed to heat under the lamp for >30 min until the spectral maximum stabilizes (between 600 and 800 cm^{-1}), and the calculated brightness temperature at the CF is near 350 K with accuracy within a mineral set of 10 K and between minerals of ~15 K, temperature ranges shown to produce less than ~0.003 variation in emissivity (Glotch et al., 2018). A temperature of 350 K was chosen as the target brightness temperature as it is a reasonable surface temperature but not the most extreme reached at equatorial noon of ~400 K (Williams et al., 2017), especially since PARSEC has a relatively high incidence angle (55°), which generally corresponds to midlatitude nonnoon measurements. Measurements of a black body target in PARSEC are acquired at 330 ± 0.5 K and 370 ± 0.5 K (to bracket the target brightness temperature of 350 K) at the beginning of each mineral series of measurements for use in calibration.

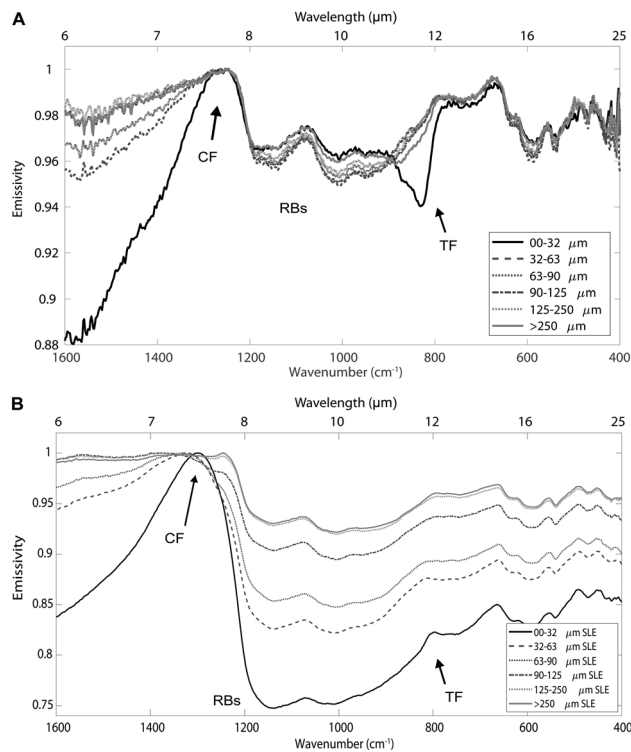


Figure 7. Mid-infrared emissivity spectra of labradorite measured under ambient conditions (a) and simulated lunar environment conditions (b) with variation in particle size. Christiansen feature (CF), Reststrahlen bands (RBs), and transparency features (TF) are labeled. The features between 1400 and 1600 cm^{-1} in (a) are due to water vapor in the chamber atmosphere.

System stability and repeatability tests have shown $<3\%$ absolute variability in spectral emissivity across the examined 1600–400 cm^{-1} spectral range for the procedures described (Figure 2). Additionally, our data are comparable to those measured at the Oxford Simulated Lunar Environment Chamber (SLEC). Figure 3 shows Miyake-jima anorthite measured in PARSEC and that measured in SLEC (Arnold et al., 2016) in which the spectra show the same positions of features with only a difference in spectral contrast in the RB regions due to the SLEC spectrum having a smaller change in brightness temperature between the CF and RBs, ~ 30 K for the PARSEC spectrum, and ~ 10 K for the SLEC spectrum.

3.3. Data Analysis

Emission spectra acquired under ambient conditions are calibrated according to the methods of Ruff et al. (1997), while spectra acquired under SLE conditions are calibrated using the similar methods of Thomas et al. (2012) but which account for the cold environment. This calibration uses a two-temperature black body method to account for the instrument response function and incorporates the chamber temperature to convert sample radiance to brightness temperature between 1600 and 800 cm^{-1} . The brightness temperature maximum is then used to convert to emissivity by setting the location of the maximum equal to 1 (further explanation of the calibration function: <http://davinci.asu.edu/index.php?title=emcal2>).

A polynomial was fit to the ~ 1100 – 1400 cm^{-1} portion of each spectrum (range dependent on mineral for best fitting), and the frequency of the maximum of the fit was used to define the CF position in the manner of Donaldson Hanna, Thomas, et al. (2012). The polynomial fitting produced errors in the small size fractions of ± 2 cm^{-1} , increasing to ± 10 cm^{-1} in the larger size fractions due to increasing asymmetry in the spectra at the CF position. To examine spectral contrast, the difference between the maximum emissivity at the CF and the emissivity at the first major RB minimum longward of the CF was used to determine changes in band depth due to particle size. Because TFs are not always present, comparisons were made by finding the frequency of the TF minimum in the smallest particle size fraction (where TF are most prominent) measured under ambient conditions and extracting the emissivity at this wavelength in all other size fractions per mineral.

maximum emissivity at the CF and the emissivity at the first major RB minimum longward of the CF was used to determine changes in band depth due to particle size. Because TFs are not always present, comparisons were made by finding the frequency of the TF minimum in the smallest particle size fraction (where TF are most prominent) measured under ambient conditions and extracting the emissivity at this wavelength in all other size fractions per mineral.

4. Results

Here we describe the spectral results for each mineral including feature positions and variations between ambient and SLE conditions as well as between particle size fractions. A summary of all feature positions, emissivity, and associated brightness temperature can be found in Table 2.

4.1. Quartz

Quartz (Figure 4) under SLE conditions shows the familiar RB features we observe under ambient conditions, notably the doublet between 1200 and 1100 cm^{-1} (Christensen et al., 2000; Mustard & Hays, 1997; Spitzer & Kleinman, 1961). The spectral contrast of these features varies with particle size between 0.566 and 0.712 emissivity at 1211 cm^{-1} , with the larger size fractions having the least spectral contrast, that is, emitting more at a value of 0.712. While the range in spectral contrast is similar between SLE (0.146) and ambient (0.168), the trend is opposite to that typically seen in thermal emission spectra acquired under ambient conditions (e.g., Salisbury & Wald, 1992). The TFs (short of 1400 cm^{-1} and near ~ 900 cm^{-1}) become more prominent with decreasing grain size in both the ambient and SLE spectra, with spectral contrast increasing from 0.040 to 0.121 under ambient conditions and 0.078 to 0.300 under SLE conditions at 900 cm^{-1} . The ambient CF position for all particle sizes is $\sim 1354 \pm 4$ cm^{-1} , and though less obvious as a single peak under SLE, shows a shift to shorter frequencies, and a variation with particle size of ~ 30 cm^{-1} . The

Table 2

Positions, Brightness Temperatures, Emissivity of the CF, First RB, and TF, and Spectral Contrast for all Minerals and Particle Sizes, the Lamp Setting for the SLE Measurements, and the Visible Albedo of the Smallest Size Fraction

Particle size	Tb-CF (K)	Tb-RB1 (K)	Tb-TF (K)	CF position (cm ⁻¹)	RB1 position (cm ⁻¹)	RB1 emissivity	RB spectral contrast	TF position (cm ⁻¹)	TF emissivity	TF spectral contrast	Light current (A)
Quartz											
Ambient											
<32	346.46	339.32	341.22	1354.0	1211.1	0.81180	0.18820	900.0	0.87894	0.12106	
32–63	347.57	337.24	344.59	1358.0	1211.1	0.74790	0.25210	900.0	0.93064	0.06936	
63–90	349.36	335.27	347.06	1357.0	1211.1	0.67390	0.32610	900.0	0.94805	0.05195	
90–125	349.21	335.11	347.08	1358.0	1211.1	0.67320	0.32680	900.0	0.95178	0.04822	
125–250	351.72	337.45	349.86	1357.0	1211.1	0.67600	0.32400	900.0	0.96032	0.03968	
>250	351.53	335.45	349.65	1350.0	1211.1	0.64330	0.35670	900.0	0.95967	0.04033	
SLE											
<32	362.72	328.90	331.36	1394.0	1211.1	0.60730	0.39270	900.0	0.70001	0.29999	6
32–63	353.92	320.85	328.70	1404.0	1211.1	0.59790	0.40210	900.0	0.74487	0.25513	6.2
63–90	358.30	321.73	335.85	1415.0	1211.1	0.56620	0.43380	900.0	0.77096	0.22904	6.4
90–125	364.57	330.25	344.91	1422.0	1211.1	0.60040	0.39960	900.0	0.80430	0.19570	6.8
125–250	351.26	327.21	340.86	1410.0	1211.1	0.68800	0.31200	900.0	0.88570	0.11430	6.9
>250	355.50	333.23	348.60	1394.0	1211.1	0.71190	0.28810	900.0	0.92151	0.07849	7.5
Anorthite											
Ambient											
<32	338.21	336.97	334.99	1237.0	1143.6	0.98120	0.01880	815.0	0.91474	0.08526	
32–63	350.03	340.11	340.10	1240.0	1143.6	0.97780	0.02220	815.0	0.96127	0.03873	
63–90	341.61	339.72	339.97	1240.0	1143.6	0.97760	0.02240	815.0	0.96729	0.03271	
90–125	341.26	346.94	347.81	1238.0	1143.6	0.96950	0.03050	815.0	0.97056	0.02944	
125–250	349.14	347.93	348.56	1240.0	1143.6	0.97130	0.02870	815.0	0.96866	0.03134	
SLE											
<32	366.56	338.00	337.34	1275.0	1143.6	0.68030	0.31970	815.0	0.74545	0.25455	7.2
32–63	364.71	344.06	343.73	1294.0	1143.6	0.75930	0.24070	815.0	0.81215	0.18785	7.1
63–90	364.41	348.07	348.50	1323.0	1143.6	0.80290	0.19710	815.0	0.85199	0.14801	6.8
90–125	361.17	349.36	349.74	1400.0	1143.6	0.85550	0.14450	815.0	0.89299	0.10701	6.5
125–250	358.25	350.49	350.45	1410.0	1143.6	0.90220	0.09780	815.0	0.92552	0.07448	6.6
Albite											
Ambient											
<32	342.68	340.68	339.34	1284.4	1186.0	0.94654	0.05347	833.1	0.91870	0.08130	
32–63	348.84	346.05	346.69	1286.3	1186.0	0.93313	0.06687	833.1	0.95317	0.04684	
63–90	343.35	341.10	340.56	1288.2	1186.0	0.94041	0.05959	833.1	0.93304	0.06696	
90–125	350.29	347.64	347.82	1286.3	1186.0	0.93813	0.06187	833.1	0.94776	0.05224	
125–250	352.15	349.09	349.90	1284.4	1186.0	0.93019	0.06981	833.1	0.95357	0.04643	
>250	350.06	346.54	348.46	1286.3	1186.0	0.91726	0.08275	833.1	0.96544	0.03456	
SLE											
<32	368.23	339.56	340.27	1317.2	1141.7	0.68165	0.31836	833.1	0.75211	0.24789	6.8
32–63	362.38	333.76	336.22	1322.9	1141.7	0.67339	0.32661	833.1	0.76029	0.23971	6.9
63–90	369.93	338.51	341.01	1322.9	1141.7	0.65743	0.34257	833.1	0.74621	0.25380	6.9
90–125	362.19	336.27	338.78	1328.7	1141.7	0.70060	0.29940	833.1	0.78377	0.21624	6.9
125–250	358.95	338.30	341.38	1342.2	1141.7	0.75255	0.24745	833.1	0.83271	0.16730	7.2
>250	358.94	352.43	354.88	1348.0	1141.7	0.87983	0.12018	833.1	0.92978	0.07022	7.2
Labradorite											
Ambient											
<32	340.95	339.74	338.63	1260.0	1141.7	0.96549	0.03451	831.2	0.94031	0.05969	
32–63	344.33	342.66	343.31	1260.0	1141.7	0.95641	0.04360	831.2	0.97514	0.02486	
63–90	340.25	338.83	339.38	1256.0	1141.7	0.95992	0.04008	831.2	0.97706	0.02294	
90–125	343.78	342.22	342.79	1257.0	1141.7	0.95891	0.04109	831.2	0.97554	0.02446	
125–250	343.07	341.65	342.14	1256.0	1141.7	0.96142	0.03858	831.2	0.97600	0.02400	
>250	345.07	343.73	343.79	1254.0	1141.7	0.96529	0.03471	831.2	0.96952	0.03048	
SLE											
<32	357.51	336.43	336.19	1297.9	1141.7	0.74775	0.25225	831.2	0.80197	0.19803	5.2
32–63	357.23	343.11	343.69	1324.9	1141.7	0.82591	0.17409	831.2	0.87166	0.12834	5

Table 2 (continued)

Particle size	Tb-CF (K)	Tb-RB1 (K)	Tb-TF (K)	CF position (cm ⁻¹)	RB1 position (cm ⁻¹)	RB1 emissivity	RB spectral contrast	TF position (cm ⁻¹)	TF emissivity	TF spectral contrast	Light current (A)
63–90	350.55	339.20	339.26	1328.7	1141.7	0.85360	0.14640	831.2	0.88711	0.11289	4.8
90–125	351.19	343.87	344.08	1363.4	1141.7	0.90387	0.09613	831.2	0.92907	0.07093	4.8
125–250	353.66	348.30	348.48	1307.0	1141.7	0.92853	0.07147	831.2	0.94763	0.05237	5
>250	354.44	349.05	349.21	1245.8	1141.7	0.93050	0.06950	831.2	0.94897	0.05103	4.8
Augite											
Ambient											
<32	340.42	338.52	337.52	1180.0	1116.7	0.94676	0.05325	738.6	0.92679	0.07321	
32–63	341.13	337.37	339.80	1185.0	1116.7	0.89924	0.10076	738.6	0.96686	0.03314	
63–90	341.00	337.31	339.91	1185.0	1116.7	0.89495	0.10505	738.6	0.97236	0.02764	
90–125	343.42	339.20	342.26	1186.0	1116.7	0.89131	0.10869	738.6	0.97188	0.02813	
125–250	342.67	338.13	341.60	1188.0	1116.7	0.88033	0.11967	738.6	0.97223	0.02777	
SLE											
<32	353.24	343.66	343.14	1191.8	1116.7	0.87898	0.12102	738.6	0.90782	0.09218	5.2
32–63	356.71	343.55	348.90	1220.7	1116.7	0.83875	0.16125	738.6	0.93072	0.06928	4.7
63–90	354.66	343.43	348.97	1234.2	1116.7	0.85998	0.14002	738.6	0.94871	0.05129	4.7
90–125	352.64	341.77	347.74	1236.2	1116.7	0.86287	0.13714	738.6	0.95537	0.04463	4.7
125–250	351.36	342.00	348.16	1236.2	1116.7	0.87977	0.12024	738.6	0.96967	0.03033	4.5
Enstatite											
Ambient											
<32	342.51	340.57	340.63	1183.0	1053.0	0.94924	0.05076	796.5	0.95369	0.04631	
32–63	345.32	341.35	343.95	1184.0	1053.0	0.90267	0.09733	796.5	0.96789	0.03211	
63–90	344.92	340.69	343.73	1186.0	1053.0	0.89511	0.10489	796.5	0.97135	0.02865	
90–125	345.82	341.44	344.47	1187.0	1053.0	0.89452	0.10549	796.5	0.96938	0.03062	
125–250	345.89	341.16	344.72	1189.0	1053.0	0.88500	0.11500	796.5	0.97216	0.02784	
>250	345.40	341.31	344.37	1190.0	1053.0	0.89896	0.10104	796.5	0.97485	0.02515	
SLE											
<32	350.84	338.40	339.60	1197.6	1053.0	0.85128	0.14872	796.5	0.89308	0.10692	4.6
32–63	354.18	341.21	345.07	1230.4	1053.0	0.84793	0.15208	796.5	0.91446	0.08554	4.6
63–90	352.84	340.57	345.40	1238.1	1053.0	0.85457	0.14543	796.5	0.92914	0.07086	4.5
90–125	350.84	340.47	345.22	1240.0	1053.0	0.87500	0.12500	796.5	0.94574	0.05426	4.5
125–250	353.63	344.57	350.16	1236.2	1053.0	0.89203	0.10797	796.5	0.96693	0.03307	4.5
>250	354.39	346.39	351.52	1240.0	1053.0	0.90465	0.09535	796.5	0.97272	0.02728	4.5
Diopside											
Ambient											
<32	340.87	338.58	339.62	1182.0	1114.7	0.92028	0.07972	761.8	0.95217	0.04783	
32–63	343.20	339.18	342.19	1190.0	1114.7	0.89545	0.10455	761.8	0.96814	0.03186	
63–90	346.99	341.76	345.77	1192.0	1114.7	0.87379	0.12621	761.8	0.97480	0.02520	
90–125	347.78	342.18	346.58	1195.0	1114.7	0.86688	0.13312	761.8	0.97215	0.02785	
125–250	345.95	340.35	345.05	1195.0	1114.7	0.86255	0.13746	761.8	0.97310	0.02690	
>250	348.25	341.98	347.20	1195.0	1114.7	0.85302	0.14698	761.8	0.98364	0.01636	
SLE											
<32	352.94	339.99	340.65	1216.0	1114.7	0.83911	0.16089	761.8	0.88814	0.11186	5.1
32–63	351.59	335.47	338.63	1232.0	1114.7	0.80016	0.19984	761.8	0.88087	0.11913	5.1
63–90	349.55	331.47	336.09	1251.6	1114.7	0.77652	0.22348	761.8	0.87598	0.12402	5.2
90–125	352.48	337.80	343.17	1288.2	1114.7	0.81725	0.18275	761.8	0.91362	0.08638	5.2
125–250	352.07	339.28	345.45	1301.0	1114.7	0.83955	0.16045	761.8	0.93816	0.06184	5.2
>250	354.02	343.27	350.51	1230.0	1114.7	0.86465	0.13535	761.8	0.96639	0.03361	5
Forsterite											
Ambient											
<32	343.36	340.46	339.75	1123.0	1054.9	0.92563	0.07437	771.4	0.91403	0.08597	
32–63	353.23	347.15	351.55	1127.0	1054.9	0.87034	0.12966	771.4	0.96653	0.03347	
63–90	350.99	345.31	349.54	1130.0	1054.9	0.87204	0.12796	771.4	0.96861	0.03139	
90–125	352.06	345.50	350.48	1148.0	1054.9	0.85523	0.14477	771.4	0.96661	0.03339	
125–250	352.63	346.12	351.14	1148.0	1054.9	0.85774	0.14226	771.4	0.96915	0.03085	
SLE											
<32	363.20	347.93	343.08	1141.7	1054.9	0.82862	0.17138	771.4	0.82339	0.17661	6.2

Table 2 (continued)

Particle size	Tb-CF (K)	Tb-RB1 (K)	Tb-TF (K)	CF position (cm ⁻¹)	RB1 position (cm ⁻¹)	RB1 emissivity	RB spectral contrast	TF position (cm ⁻¹)	TF emissivity	TF spectral contrast	Light current (A)
32–63	368.11	348.90	350.33	1151.3	1054.9	0.79238	0.20762	771.4	0.84649	0.15351	5.8
63–90	361.63	346.72	349.33	1153.2	1054.9	0.83184	0.16816	771.4	0.89066	0.10934	5.8
90–125	367.36	351.47	356.18	1174.0	1054.9	0.82595	0.17405	771.4	0.90296	0.09704	5.6
125–250	364.88	352.18	357.90	1170.0	1054.9	0.85744	0.14256	771.4	0.93791	0.06209	5.4
Ilmenite											
Ambient											
<32	348.36	347.22		786.8	680.8	0.97560	0.02440				
32–63	349.15	346.40		808.0	680.8	0.94242	0.05758				
63–90	394.26	389.84		811.9	680.8	0.94703	0.05297				
90–125	393.43	387.99		810.0	680.8	0.93504	0.06497				
125–250	393.32	387.25		806.1	680.8	0.92763	0.07237				
SLE											
<32	358.46	355.20		804.2	680.8	0.97256	0.02744				4.4
32–63	357.73	350.81		808.0	680.8	0.94181	0.05819				4.4
63–90	358.40	350.90		806.1	680.8	0.93836	0.06164				4.5
90–125	351.64	345.18		804.2	680.8	0.94508	0.05492				4.4
125–250	356.73	349.84		806.1	680.8	0.94303	0.05697				4.5

Note. CF = Christiansen feature; RB = Reststrahlen bands; TF = transparency features; SLE = simulated lunar conditions.

features shortward of the CF in these and other ambient spectra are due to atmospheric water due to being measured with ambient lab air in the chamber.

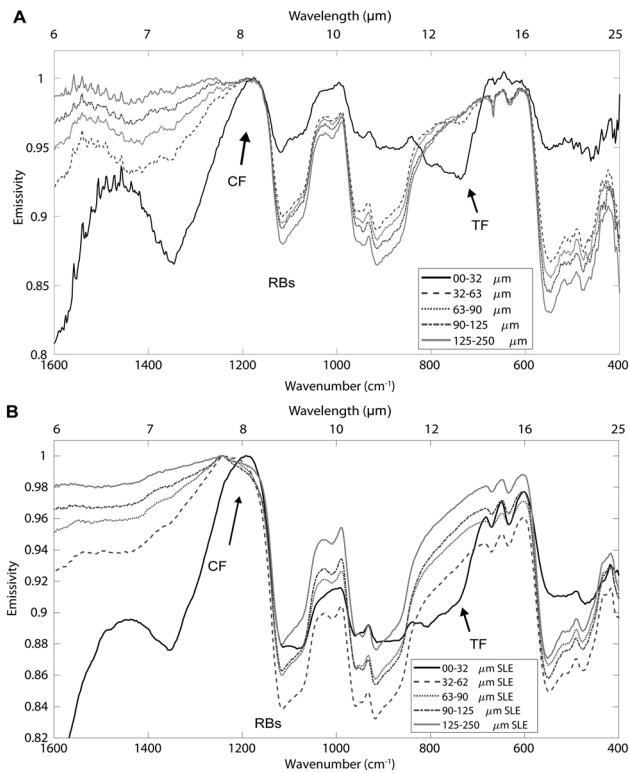


Figure 8. Mid-infrared emissivity spectra of augite with varying particle size measured under ambient conditions (a) and simulated lunar environment conditions (b). Christiansen feature (CF), Reststrahlen bands (RBs), and transparency features (TF) are labeled. The features between 1300 and 1600 cm⁻¹ in (a) are due to water vapor in the chamber atmosphere.

4.2. Feldspars

Anorthite RBs under ambient conditions show decreasing spectral contrast with decreasing particle size (a change of 0.012 emissivity at 1144 cm⁻¹), while under SLE show increasing spectral contrast with decreasing particle size from 0.075 to 0.255 at 1144 cm⁻¹ (Figure 5). The TFs become more prominent with decreasing particle size shortward of 1240 cm⁻¹, and especially for the <32 μm size fraction at 815 cm⁻¹ under ambient conditions increasing by 0.054 at 815 cm⁻¹ from the largest size fraction band depth. The TFs show similar trends under SLE conditions going from 0.926 emissivity for the 125- to 250-μm fraction to 0.745 emissivity for the <32-μm fraction at 815 cm⁻¹, though this TF is less pronounced due to the higher overall spectral contrast of the SLE spectra. The SLE CF position shifts to shorter frequency compared to ambient by 36 cm⁻¹ for the <32-μm-size fraction, and more so with increasing particle size, up to 170 cm⁻¹ for the 125- to 250-μm fraction. Overall, there is a significant increase in spectral contrast between SLE and ambient spectra with the difference between the CF and first RB increasing by 0.320 for the smallest size fraction under SLE.

Albite ambient spectra show RB spectral contrast variation with particle size of 0.029, and band depth of the 833 cm⁻¹ TF varying by 0.047, though the occurrence of this TF in larger size fractions likely indicates the presence of clinging fines as long wavelength TFs are not seen in the larger size fractions of the other minerals (Figure 6a). Under SLE, the RBs increase in spectral contrast from 0.120 to 0.343 with decreasing particle size, except for the two smallest size fractions, which have contrast of 0.327 (32–63 μm) and 0.318 (<32 μm; Figure 6b). The SLE TFs are less prominent than under ambient conditions but also decrease in emissivity from 0.930 to 0.752 at 833 cm⁻¹ with decreasing particle size. The SLE CF position shifts between 1317 cm⁻¹ (<32 μm) and 1248 cm⁻¹

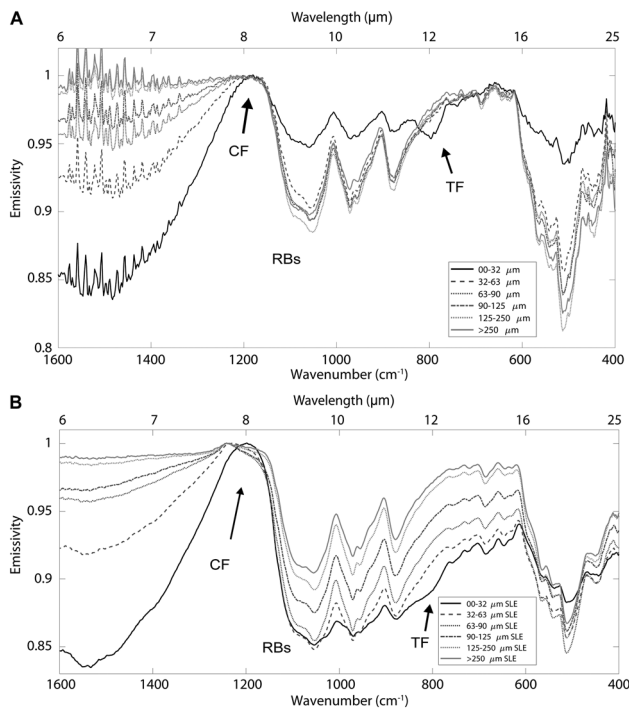


Figure 9. Mid-infrared emissivity spectra of enstatite with varying particle size measured under ambient conditions (a) and simulated lunar environment conditions (b). Christiansen feature (CF), Reststrahlen bands (RBs), and transparency features (TF) are labeled. The features between 1300 and 1600 cm^{-1} in (a) are due to water vapor in the chamber atmosphere.

ward of the CF increases in spectral contrast with decreasing particle size in both ambient and SLE, but the TF at 738 cm^{-1} is only present in the two smallest size fractions under ambient and in the smallest under SLE. The CF position has little shift between ambient and SLE, only $\sim 10 \text{ cm}^{-1}$ in the smallest size fraction, though under SLE the CF shifts an additional $\sim 30 \text{ cm}^{-1}$ to shorter wavelengths with increasing particle size.

As with augite, enstatite shows little shift in spectral contrast within the RBs, only 0.017 variation at 1053 cm^{-1} and lacks a TF at 796 cm^{-1} except for the smallest size fraction under ambient conditions (Figure 9a). Under SLE conditions, spectral contrast increases with decreasing particle size from 0.120 to 0.161 at 1053 cm^{-1} , except for the smallest size fraction which has contrast of 0.121 (Figure 9b). The TFs are also more prominent with decreasing particle size short of the CF in both the ambient and SLE conditions, though the TF at 796 cm^{-1} only appears in the smallest size fraction. The CF shifts from $\sim 1187 \text{ cm}^{-1}$ under ambient to lower frequency with increasing particle size from 1197 cm^{-1} to 1240 cm^{-1} under SLE, but stays relatively consistent for sizes fractions greater than $63 \mu\text{m}$ with only 4 cm^{-1} variability.

Diopside also shows decreasing spectral contrast with decreasing particle size under ambient conditions from 0.147 to 0.080 at 1115 cm^{-1} and a steady increase in spectral contrast of the TF shortward of 1180 cm^{-1} and most prominent at 762 cm^{-1} in the $<32 \mu\text{m}$ size fraction (Figure 10a). The SLE spectra show increasing spectral contrast with decreasing particle size from 0.135 to 0.223, until the 32- to $63 \mu\text{m}$ size fraction where it begins decreasing in contrast to 0.161 for the $<32 \mu\text{m}$ size fraction (Figure 10b). The TFs become more prominent with decreasing particle size short of the CF, but is only notable at 762 cm^{-1} in the smallest size fraction. The SLE CF position is at shorter frequencies than under ambient conditions (1192 cm^{-1}), and generally shifts to shorter frequencies with increasing particle size from 1216 cm^{-1} for $<32 \mu\text{m}$ to 1301 cm^{-1} for $125\text{--}250 \mu\text{m}$, save for the largest size fraction with a CF at 1230 cm^{-1} .

4.4. Olivine

Forsterite ambient spectra show a decrease in spectral contrast with decreasing particle size from 0.142 to 0.074 at 1055 cm^{-1} under ambient conditions, while the SLE spectra show an increase in spectral contrast

($>250 \mu\text{m}$), but is relatively consistent in the size fractions $<125 \mu\text{m}$ with only $\sim 10 \text{ cm}^{-1}$ variation, though all are at shorter frequencies by at least 36 cm^{-1} than the ambient CF position. Overall spectral contrast has increased by ~ 0.25 between the CF and first RB of the smallest size fraction under SLE.

The ambient spectra of labradorite are relatively similar aside from the smallest size fraction, which shows significant increases in the contrast of the TFs shortward of 1350 cm^{-1} and near 830 cm^{-1} decreases in emissivity by 0.035 from the next largest size fraction (Figure 7a). Under SLE, the largest two size fractions of labradorite are about the same, then spectral contrast of the RB increases with decreasing particle size from 0.070 to 0.252 at 1142 cm^{-1} . The SLE TFs increase in spectral contrast shortward of $\sim 1350 \text{ cm}^{-1}$ but only barely appear near 830 cm^{-1} in the smallest size fraction though emissivity has decreased with decreasing particle size at this wave number (Figure 7b). The SLE CF position shows a shift to shorter frequencies than at ambient by $\sim 25 \text{ cm}^{-1}$, and has a range of $\sim 70 \text{ cm}^{-1}$ with the shortest position for the 63- and $90 \mu\text{m}$ size fraction, the largest three size fractions exhibiting a shoulder at 1245 cm^{-1} which is taken as the CF position for the largest size fraction.

4.3. Pyroxenes

Augite shows little variation in spectral contrast in the RBs under ambient conditions increasing in emissivity from 0.880 to 0.899 at 1117 cm^{-1} with decreasing particle size, except in the smallest size fraction which jumps to 0.947. Under SLE the RBs decrease in emissivity with decreasing particle size from 0.880 to 0.839, but the smallest size fraction again differs by increasing in emissivity to 0.879 at 1117 cm^{-1} (Figure 8). The TF short-

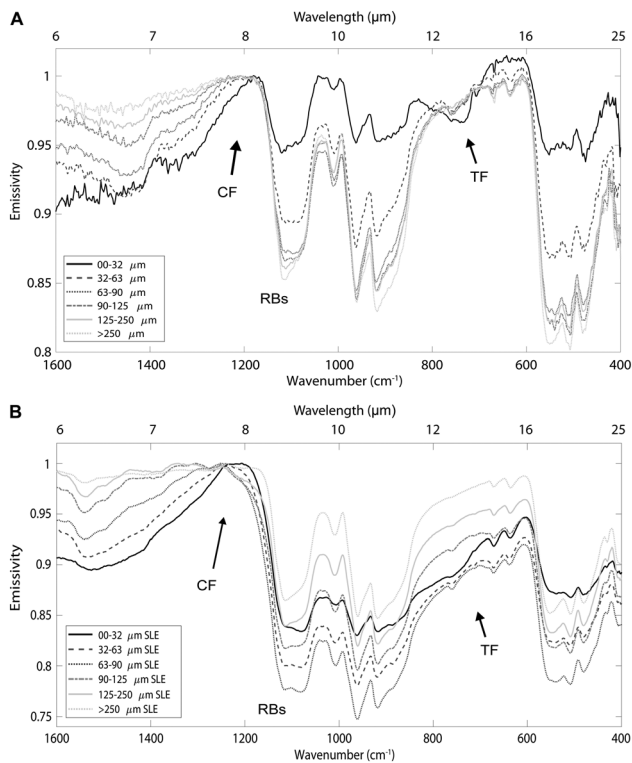


Figure 10. Mid-infrared emissivity spectra of diopside with varying particle size measured under ambient conditions (a) and simulated lunar environment conditions (b). Christiansen feature (CF), Reststrahlen bands (RBs), and transparency features (TF) are labeled. The features between 1300 and 1600 cm^{-1} in (a) are due to water vapor in the chamber atmosphere.

with decreasing particle size from 0.143 to 0.208, with the exception of the smallest size fraction which decreases in contrast to 0.171 (Figure 11). The TF shortward of the CF becomes more pronounced with decreasing particle size, and the TF at 771 cm^{-1} appears only in the $<32\text{-}\mu\text{m}$ size fraction for both ambient and SLE spectra. The CF shifts $\sim 20 \text{ cm}^{-1}$ from ambient at $\sim 1123 \text{ cm}^{-1}$ to SLE at 1142 cm^{-1} for the smallest size fraction and moves $\sim 40 \text{ cm}^{-1}$ to lower frequencies with increasing particle size to 1170 cm^{-1} for the $125\text{--}250 \mu\text{m}$.

4.5. Ilmenite

While not a silicate, ilmenite is a major mineral in some mare basalts on the lunar surface (e.g., McKay & Williams, 1979; Rutherford et al., 1980). The Fe/Ti-O vibrational modes at wavelengths $> \sim 12 \mu\text{m}$ show decreasing spectral contrast with decreasing particle size from 0.072 to 0.024 under ambient conditions and from 0.057 to 0.027 under SLE conditions at 680 cm^{-1} . There is almost no variation in TF prominence short of the CF or change in CF position between ambient and SLE conditions, both at $\sim 805 \text{ cm}^{-1}$ (Figure 12).

5. Discussion

5.1. Spectral Trends

The mineral spectra that we acquired show the typical behaviors observed under ambient conditions, which include a definitive CF position, an increase in emissivity in the RBs, and the emergence of TFs with decreasing particle size (e.g., Hamilton, 2000; Lyon, 1964; Mustard & Hays, 1997; Salisbury & Eastes, 1985; Salisbury et al., 1987; Salisbury & Wald, 1992; Vincent & Hunt, 1968). Our SLE spectra show a shift in the CF position to shorter wavelengths when compared to ambient CF positions and an overall increase in spectral contrast (Figure 13), as has been shown in

numerous studies (e.g., Donaldson Hanna, Thomas, et al., 2012; Henderson & Jakosky, 1994, 1997; Logan & Hunt, 1970).

Our study shows that CF position under SLE can also shift as a function of particle size which is consistent with previous studies by Logan and Hunt (1970), Logan et al. (1973), and Henderson and Jakosky (1997). The observed shift is significant, over 100 cm^{-1} ($0.5 \mu\text{m}$) in anorthite and at least 20 cm^{-1} ($0.12 \mu\text{m}$) in all silicates. Additionally, the RBs under SLE do not exhibit the same trend of increasing emissivity with decreasing particle size as under ambient conditions but generally decrease in emissivity with decreasing particle size, without shifting in position. TFs under SLE appear with decreasing particle size, especially short of the CF, though their prominence at longer wavelengths is often less in the SLE spectra due to overall increase in spectral contrast, and do not shift in position.

While the CF positions of all the silicates measured in this study shift to some degree, we observe the strongest shifts between ambient and SLE in the quartz and the feldspars and least in the pyroxenes (apart from diopside; Figure 13). The feldspars and quartz also have the largest variation with particle size. We can speculate that the larger variation is likely due to the mineral visible albedo (Donaldson Hanna et al., 2017; Henderson & Jakosky, 1994; Logan et al., 1973; Lucey et al., 2017; Shirley et al., 2018). Visible albedo is measured as the reflectance at 750 nm as that is a location used in other works (e.g., Lucey et al., 2017) and is listed for the smallest size fraction in the supporting information S1. The darker pyroxenes have less variation in the CF position, due to a shallower observed thermal gradient within these samples (Table 2). The slightly brighter olivine and much brighter feldspars have larger CF shifts and begin to have less well-defined CF positions in the larger size fractions, likely due again to the differences in thermal gradient, for these less absorbing materials. Of note is the more pronounced difference in CF position among the pyroxenes under SLE when compared to their almost indistinguishability under ambient conditions, seen best in the smallest size fraction in Figure 13b.

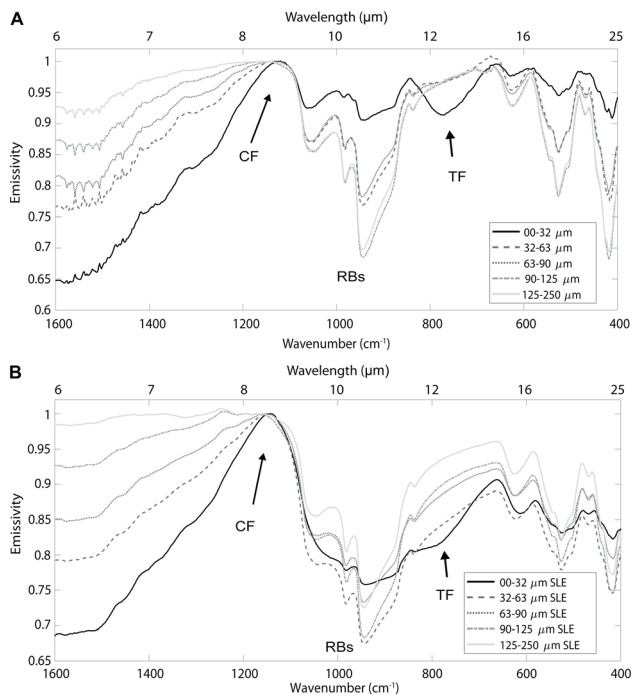


Figure 11. Mid-infrared emissivity spectra of olivine with varying particle size measured under ambient conditions (a) and simulated lunar environment conditions (b). Christiansen feature (CF), Reststrahlen bands (RBs), and transparency features (TF) are labeled.

In general, our SLE samples show a steep decrease in emissivity in the RBs with decreasing particle size, the opposite of the trend we observe under terrestrial ambient conditions (Figure 14a), though in half the silicates the smallest two-size fractions are similar or begin to increase in emissivity compared to the 90–125 μm fraction. The trend of decreasing emissivity under SLE has been observed in Donaldson Hanna, Thomas, et al. (2012); however, the change with particle size was only noted in an early study (Logan & Hunt, 1970) on limited samples. The decrease is likely due to the thermal gradient in the regolith and that the RBs, where the extinction coefficient (k) is high, are sampling from the cooler upper regions of the regolith, limiting the depth of sensitivity in this region. There is generally >10 K difference in brightness temperature between the CF and RB1 with greater differences in the smaller size fractions, as seen in Table 2, thus it is likely that the smaller size fractions are more influenced by the thermal gradient. This is logical as the largest size fractions have particles that begin to approach the depth to which the gradient is present, whereas the smaller particle sizes have more particles spanning the same depth. Additionally, the wavelength of the incident light is less than the particle size of the samples, meaning the light is not penetrating far into the sample.

While this SLE RB trend generally holds, it is not constant in all samples, nor is the depth of the band unique to a particle size. We expect that sample preparation and porosity may play a role in the trends we observed (e.g., Donaldson Hanna, Wyatt, et al., 2012; Salisbury & Eastes, 1985) and have assessed the sample preparation to produce spectra to within 3% absolute variability in emissivity, while experiments

changing the vacuum pump down rate to exert some control on porosity of sample have also shown variability of $<3\%$ emissivity (Shirley, 2018). While this does affect the degree of spectral contrast in our spectra, the effect is inconsistent, and it is difficult to quantify the pump rate and its physical effect on the sample as we cannot directly measure porosity. Logan et al. (1973) did demonstrate the importance of porosity, and increasing porosity should increase spectral contrast, as it will affect the thermal gradient.

TFs are due to volume scattering in the sample and are enhanced with decreasing particle size as seen in previous studies (e.g., Cooper et al., 2002). This trend remains true under SLE conditions, though it does show more spectral contrast than when measured under ambient (Figure 14b) in the same way that the RBs do. The trend is most noticeable shortward of the CF position, but the TF longward of the first RB region ($\sim 600\text{--}800$ cm^{-1} for most minerals here) is only slightly noticeable in the SLE spectra in the smallest size fractions. It is likely that the volume scattering effects remain in the SLE conditions, but the longer wavelength TF region is smaller, and the overall decrease in emissivity in the first RB region overshadows it.

Overall, particle size appears to play a major role in spectral variability, likely due to the thermal gradient that can be achieved in each size fraction. The smallest size fractions are most susceptible to steeper gradients, creating the greater spectral contrast. Additionally, in comparing anorthite measured in PARSEC (<32 μm) to that measured in SLEC (<63 μm ; Figure 3), the positions of features are the same, including the CF and the prominence of the 815 cm^{-1} TF despite variation in the upper limit of the size fraction, which points to the finest particles having a greater influence on the resulting spectrum. The difference in contrast relates to the gradient variation, which is much smaller in the SLEC spectrum (~ 10 K compared to ~ 30 K in PARSEC). It is unclear if this is due to variation in the particle size distribution of the <63 μm anorthite or difference in measurement procedure.

Another indicator that the fine particles have a strong influence is seen in the albite spectra in this study, which show the 833 cm^{-1} TF appearing in multiple-size fractions in the ambient spectra, likely indicating that clinging fines were not adequately removed from some of the fractions. The lack of variation in the CF under SLE, despite being a bright mineral, as well as the RB spectral contrast being only slightly

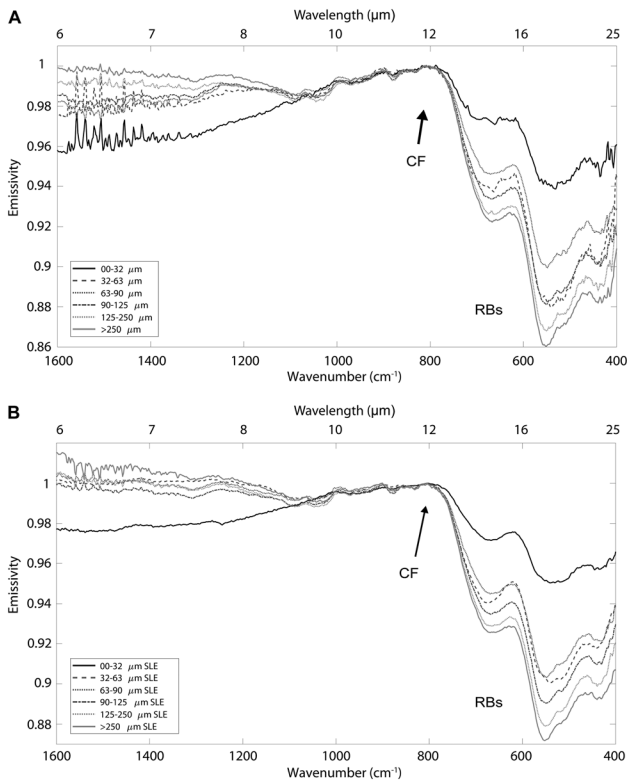


Figure 12. Mid-infrared emissivity spectra of ilmenite with varying particle size measured under ambient conditions (a) and simulated lunar environment conditions (b). Christiansen feature (CF), Reststrahlen bands (RBs), and transparency features (TF) are labeled. The features between 1400 and 1600 cm^{-1} in (a) are due to water vapor in the chamber atmosphere.

larger than error in the smallest three-size fractions, indicates that those fines have a large influence on the SLE spectra. Additionally, lower emissivity in the TF region short of the CF in the ambient spectra for the largest size fraction of forsterite and labradorite may also indicate incomplete elimination of clinging fines and contribute to the CF value under SLE being more consistent with the smaller size fractions.

5.2. Applications to Diviner Lunar Radiometer Data Analysis

From Figure 13 we see that while mineral CFs change with grain size, the trends are not consistent among the minerals. The importance of this data set is that it provides evidence that there is variation in CF position with particle size, though we can only establish a range of CF position values to be expected for a certain mineral under lunar conditions. Traditionally, previous authors have tended to treat CF position as distinct and indicative of composition, as there is little variability in the ambient CF position (e.g., Conel, 1969). Here, we observe that CF positions of certain minerals cross the ranges of others, depending on size fraction. The variability of CF position with particle size points to the complications in mineral identification when using it as the sole indicator of composition. The variability of CF position with size fraction complicates our interpretation of mineralogy from remote sensing and demonstrates the importance of MIR hyperspectral instruments for analysis of airless bodies, which, in addition to CF position, would also provide more information about other important spectral features like the RBs and TFs.

We resampled our data to Diviner resolution (Channels 3–6) to see how much of an effect particle size makes on our interpretation of

the data set in the CF region. Figure 15 shows SLE anorthite spectra at Diviner resolution in which the particle size effects are still apparent. However, for some of the quartz, feldspar, and olivine spectra, the CF values calculated from the Diviner resolution spectra are not reasonable as they fall outside of the range

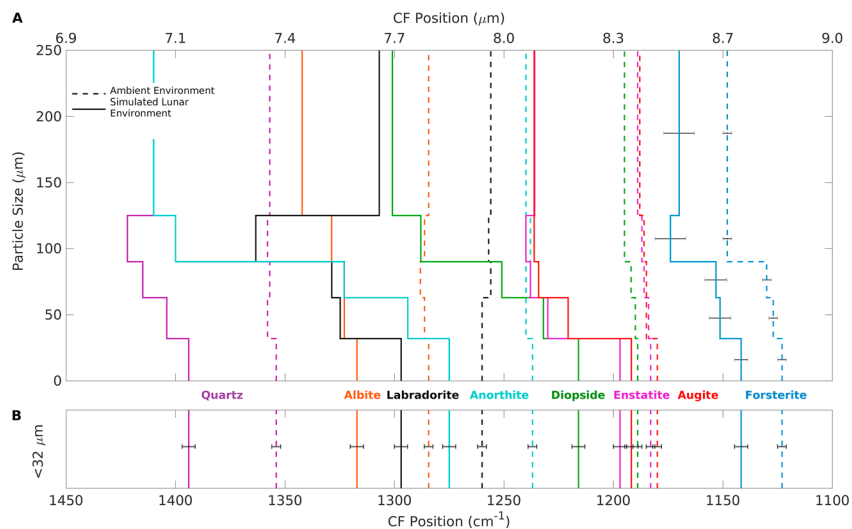


Figure 13. Variation of Christiansen feature (CF) position measured under ambient conditions (dashed lines) and simulated lunar environment conditions (solid lines) per particle size fraction (a). Panel (b) shows the smallest particle size (<32 μm) CF positions, which highlights the shift due to environmental conditions.

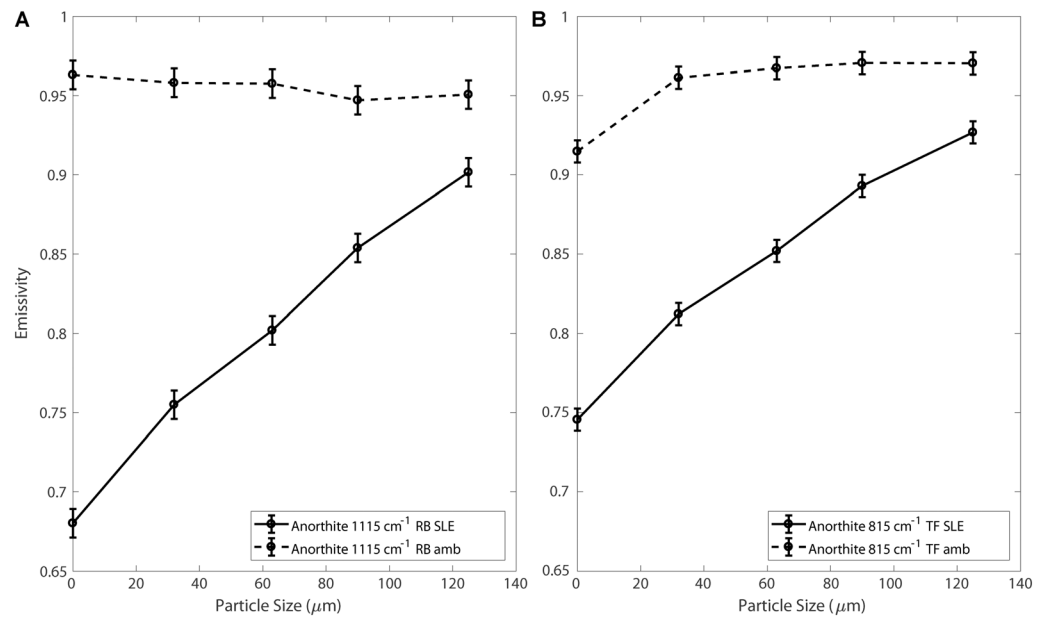


Figure 14. Variation in emissivity with particle size between ambient conditions (dashed) and simulated lunar environment (SLE) conditions (solid) for anorthite Reststrahlen bands (RB) 1115 cm^{-1} (a) and transparency features (TF) 815 cm^{-1} (b).

of the Diviner CF channels (1280–1160 cm^{-1} or 7.8–8.6 μm). These calculated CF values have been included in Table 3, but we emphasize the necessity of additional parameters to evaluate and constrain these compositions.

Glotch et al. (2010) defined spectral parameters I and c , which define the slope between 7.8 and 8.2 μm , and the concavity between 7.8 and 8.6 μm , respectively. When the other mineral spectra are resampled, the differences due to particle size are less obvious (e.g., pyroxenes), but including these additional parameters, I and c , enable us to clearly distinguish particle size variation (Table 3). These differences are within the detectable limit of Diviner spectral resolution, but perhaps less so at Diviner spatial resolution where the fine-grained nature of lunar regolith will likely dominate per pixel. While most of the Moon is dominated by fine-grained material, regions around young craters have higher rock abundance (e.g., Bandfield et al., 2011, 2017) and may have enough variation in particle size to require consideration; however, further investigation is necessary to determine the proportion of larger particle size material needed to overcome the influence of the smallest size fraction.

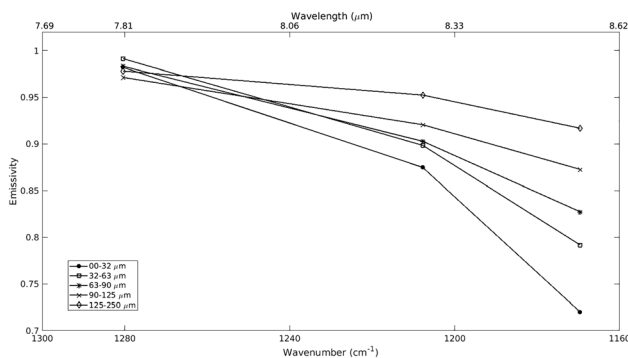


Figure 15. Anorthite simulated lunar environment mid-infrared emissivity spectra resampled to Diviner resolution within the Christiansen feature wavelength region. Note variability due to particle size is still apparent.

Additionally, highly silicic features on the Moon have been identified using the indices I and c (Glotch et al., 2010); however, these indices also change with particle size (Table 3). Figure 16 shows the anorthite (a mineral with a low-frequency CF value) spectra with the addition of channel 6, which falls within the range of our laboratory data set. Because this is a broadband channel, we cannot account for individual RBs or TFs, but including this channel allows the increase in spectral contrast to be factored into our analysis of Diviner data which may assist in distinguishing the variations due to composition or particle size in these highly silicic regions. Overall, the presence of prominent TFs at small particle sizes may contribute to a lower emissivity as observed by Diviner channel 6, so material with similar index values but with a low channel 6 emissivity may point to small particle size having a larger influence on the spectrum, thus informing us about the regolith properties as well.

Table 3
Data for the SLE Spectra at Diviner Resolution Including Both the Laboratory and Diviner Resolution CF Values, and the Indices for Slope and Concavity

Mineral	CF position (cm ⁻¹) SLE lab resolution	CF value (cm ⁻¹) Diviner resolution	Concavity index <i>c</i>	Slope index <i>I</i>
Quartz				
<32	1394	1188	0.05400	0.00142
32–63	1404	1186	0.05379	0.00154
63–90	1415	1184	0.05858	0.00178
90–125	1422	1182	0.05540	0.00177
125–250	1410	1180	0.05481	0.00183
>250	1394	1176	0.05751	0.00213
Anorthite				
<32	1275	1282	-0.06451	0.00236
32–63	1294	1303	-0.03794	0.00180
63–90	1323	1341	-0.02174	0.00141
90–125	1400	1339	-0.01395	0.00089
125–250	1410	1285	-0.01449	0.00055
Albite				
<32	1317	1116	0.02415	0.00243
32–63	1323	1126	0.02684	0.00240
63–90	1323	1113	0.02440	0.00258
90–125	1329	1101	0.01806	0.00219
125–250	1342	1084	0.01197	0.00176
>250	1348	1391	-0.01056	0.00089
Labradorite				
<32	1298	10422	-0.00724	0.00201
32–63	1325	3593	-0.00532	0.00131
63–90	1329	1528	-0.00874	0.00108
90–125	1363	1333	-0.01114	0.00069
125–250	1307	1287	-0.01367	0.00054
>250	1246	1283	-0.01433	0.00053
Augite				
<32	1192	1193	-0.02437	-0.00055
32–63	1221	1225	-0.01779	0.00003
63–90	1234	1231	-0.01207	0.00007
90–125	1236	1237	-0.01002	0.00010
125–250	1236	1243	-0.00577	0.00008
>250	1238	1243	-0.00594	0.00008
Enstatite				
<32	1198	1199	-0.02074	-0.00036
32–63	1230	1218	-0.01407	-0.00005
63–90	1238	1231	-0.00964	0.00006
90–125	1240	1231	-0.00774	0.00005
125–250	1236	1227	-0.00441	0.00001
>250	1240	1223	-0.00355	0.00000
Diopside				
<32	1216	1222	-0.02487	-0.00002
32–63	1232	1237	-0.02845	0.00028
63–90	1252	1251	-0.02771	0.00052
90–125	1288	1264	-0.01516	0.00040
125–250	1301	1272	-0.00802	0.00025
>250	1230	1233	-0.00442	0.00003
Forsterite				
<32	1142	877	-0.00070	-0.00107
32–63	1151	861	-0.00030	-0.00064
63–90	1153	1100	-0.00306	-0.00038
90–125	1174	1194	-0.00459	-0.00010
125–250	1170	1225	-0.00170	0.00000
Ilmenite				
<32	804	1276	0.00105	-0.00004
32–63	808	1336	-0.00033	0.00002
63–90	806	1243	-0.00349	0.00005
90–125	804	1244	-0.00306	0.00004

Table 3 (continued)

Mineral	CF position (cm ⁻¹) SLE lab resolution	CF value (cm ⁻¹) Diviner resolution	Concavity index <i>c</i>	Slope index <i>I</i>
125–250	806	1256	−0.00269	0.00006

Note. Diviner resolution CF values outside of 1280–1160 cm⁻¹ fall outside of the Diviner range and are not believable. SLE = simulated lunar environment; CF = Christiansen feature.

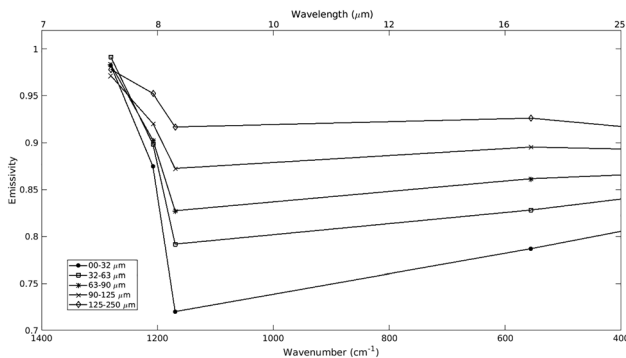


Figure 16. Anorthite simulated lunar environment mid-infrared emissivity spectra with varying particle size resampled to Diviner resolution including broadband channel 6 (13–23 μm).

6. Conclusions

Laboratory spectral databases are necessary to analyze MIR remote sensing data sets, and a database specific to the Moon and its environment is needed to best understand the Diviner and future lunar MIR instrument data. This study, which builds on earlier studies (e.g., Henderson & Jakosky, 1997; Logan et al., 1973; Logan & Hunt, 1970) investigating particle size, demonstrates the complexity of MIR emission spectra acquired on airless bodies and emphasizes the importance of measuring spectra in a simulated environment conditions. Particle size not only plays a role in the spectral contrast and sharpness of features, as it does under terrestrial conditions, but, under SLE, affects the location of one of our primary diagnostic features, the CF. This work demonstrates that particle size variations can be detected at Diviner spectral resolution, which relies on the CF for bulk silicate compositional analysis, and can potentially give us further insights into the size distribution in the regolith, though will likely be most

useful for future lunar missions at higher spatial resolutions, like landed missions. Additionally, this work emphasizes the importance of hyperspectral instruments in future missions (e.g., OSIRIS-REx and BepiColombo) to provide a better characterization of MIR spectral features and a more robust analysis of airless body regoliths.

Acknowledgments

The authors would like to thank K. Donaldson Hanna and B. Greenhagen for their comments and suggestions that helped improve this manuscript, as well as N. DiFrancesco and P. Carpenter for assistance with sample preparation and microprobe analysis. This work was supported by NASA LASER grant NNX13AK13G, the Diviner Lunar Radiometer Experiment extended science mission, and the RIS⁴E node of NASA's Solar System Exploration Research Virtual Institute. Data used in the work can be found on the Stony Brook University Academic Commons at <https://commons.library.stonybrook.edu>.

References

- Allen, C. C., Greenhagen, B. T., Hanna, K. L. D., & Paige, D. A. (2012). Analysis of lunar pyroclastic deposit FeO abundances by LRO Diviner. *Journal of Geophysical Research*, *117*, E00H28. <https://doi.org/10.1029/2011JE003982>
- Armstrong, J. T. (1995). CITZAF: A package of correction programs for the quantitative electron microbeam X-ray analysis of thick polished materials. *Thin Films, and Particles, Microbeam Analysis*, *4*, 177–200.
- Arnold, J. A., Glotch, T. D., Lucey, P. G., Song, E., Thomas, I. R., Bowles, N. E., & Greenhagen, B. T. (2016). Constraints on olivine-rich rock types on the Moon as observed by Diviner and M3: Implications for the formation of the lunar crust. *Journal of Geophysical Research: Planets*, *121*, 1342–1361. <https://doi.org/10.1002/2015JE004874>
- Ashley, J. W., Robinson, M. S., Stopar, J. D., Glotch, T. D., Hawke, B. R., van der Bogert, C. H., et al. (2016). The Lassell massif—A silicic lunar volcano. *Icarus*, *273*, 248–261. <https://doi.org/10.1016/j.icarus.2015.12.036>
- Bandfield, J. L., Cahill, J. T., Carter, L. M., Neish, C. D., Patterson, G. W., Williams, J. P., & Paige, D. A. (2017). Distal ejecta from lunar impacts: Extensive regions of rocky deposits. *Icarus*, *283*, 282–299. <https://doi.org/10.1016/j.icarus.2016.05.013>
- Bandfield, J. L., Ghent, R. R., Vasavada, A. R., Paige, D. A., Lawrence, S. J., & Robinson, M. S. (2011). Lunar surface rock abundance and regolith fines temperatures derived from LRO Diviner Radiometer data. *Journal of Geophysical Research*, *116*, E00H02. <https://doi.org/10.1029/2011JE003866>
- Bandfield, J. L., Hayne, P. O., Williams, J.-P., Greenhagen, B. T., & Paige, D. A. (2015). Lunar surface roughness derived from LRO Diviner Radiometer observations. *Icarus*, *248*, 357–372. <https://doi.org/10.1016/j.icarus.2014.11.009>
- Bennett, K. A., Horgan, B. H., Gaddis, L. R., Greenhagen, B. T., Allen, C. C., Hayne, P. O., et al. (2016). Complex explosive volcanic activity on the Moon within Oppenheimer crater. *Icarus*, *273*, 296–314. <https://doi.org/10.1016/j.icarus.2016.02.007>
- Boyce, J. M., Giguere, T., Mougini-Mark, P., Glotch, T. D., & Taylor, G. J. (2018). Geology of Mairan middle dome: Its implication to silicic volcanism on the Moon. *Planetary and Space Science*, *162*, 62–72. <https://doi.org/10.1016/j.pss.2017.12.009>
- Carrier, W. D. (1973). Lunar soil grain size distribution. *The moon*, *6*(3–4), 250–263. <https://doi.org/10.1007/BF00562206>
- Christensen, P. R., Bandfield, J. L., Hamilton, V. E., Howard, D. A., Lane, M. D., Piatek, J. L., et al. (2000). A thermal emission spectral library of rock-forming minerals. *Journal of Geophysical Research*, *105*, 9735–9739. <https://doi.org/10.1029/1998JE000624>
- Conel, J. E. (1969). Infrared emissivities of silicates: Experimental results and a cloudy atmospheric model of spectral emission from condensed particulate mediums. *Journal of Geophysical Research*, *74*, 1614–1634. <https://doi.org/10.1029/JB074i006p01614>
- Cooper, B. L., Salisbury, J. W., Killen, R. M., & Potter, A. E. (2002). Midinfrared spectral features of rocks and their powders. *Journal of Geophysical Research*, *107*(E4), 5017. <https://doi.org/10.1029/2000JE001462>
- Donaldson Hanna, K. D., Greenhagen, B. T., Patterson, W. R., Pieters, C. M., Mustard, J. F., Bowles, N. E., et al. (2017). Effects of varying environmental conditions on emissivity spectra of bulk lunar soils: Application to Diviner thermal infrared observations of the Moon. *Icarus*, *283*, 326–342. <https://doi.org/10.1016/j.icarus.2016.05.034>

- Donaldson Hanna, K. L., Cheek, L. C., Pieters, C. M., Mustard, J. F., Greenhagen, B. T., Thomas, I. R., & Bowles, N. E. (2014). Global assessment of pure crystalline plagioclase across the Moon and implications for the evolution of the primary crust. *Journal of Geophysical Research: Planets*, *119*, 1516–1545. <https://doi.org/10.1002/2013JE004476>
- Donaldson Hanna, K. L., Thomas, I. R., Bowles, N. E., Greenhagen, B. T., Pieters, C. M., Mustard, J. F., et al. (2012). Laboratory emissivity measurements of the plagioclase solid solution series under varying environmental conditions. *Journal of Geophysical Research*, *117*, E11004. <https://doi.org/10.1029/2012JE004184>
- Donaldson Hanna, K. L., Wyatt, M. B., Thomas, I. R., Bowles, N. E., Greenhagen, B. T., Maturilli, A., et al. (2012). Thermal infrared emissivity measurements under a simulated lunar environment: Application to the Diviner Lunar Radiometer Experiment. *Journal of Geophysical Research*, *117*, E00H05. <https://doi.org/10.1029/2011JE003862>
- Elder, C. M., Hayne, P. O., Bandfield, J. L., Ghent, R. R., Williams, J. P., Hanna, K. D., & Paige, D. A. (2017). Young lunar volcanic features: Thermophysical properties and formation. *Icarus*, *290*, 224–237. <https://doi.org/10.1016/j.icarus.2017.03.004>
- Glotch, T. D., Bandfield, J. L., Lucey, P. G., Hayne, P. O., Greenhagen, B. T., Arnold, J. A., et al. (2015). Formation of lunar swirls by magnetic field standoff of the solar wind. *Nature Communications*, *6*(1). <https://doi.org/10.1038/ncomms7189>
- Glotch, T. D., Edwards, C. S., Yesiltas, M., Shirley, K. A., McDougall, D. S., Kling, A. M., et al. (2018). MGS-TES spectra suggest a basaltic component in the regolith of Phobos. *Journal of Geophysical Research: Planets*, *123*, 2467–2484. <https://doi.org/10.1029/2018JE005647>
- Glotch, T. D., Hagerty, J. J., Lucey, P. G., Hawke, B., Giguere, T. A., Arnold, J. A., et al. (2011). The Marian domes: Silicic volcanic constructs on the Moon. *Geophysical Research Letters*, *38*, L21204. <https://doi.org/10.1029/2011GL049548>
- Glotch, T. D., Lucey, P. G., Bandfield, J. L., Greenhagen, B. T., Thomas, I. R., Elphic, R. C., et al. (2010). Highly silicic compositions on the Moon. *Science*, *329*(5998), 1510–1513. <https://doi.org/10.1126/science.1192148>
- Greenhagen, B. T., Lucey, P. G., Wyatt, M. B., Glotch, T. D., Allen, C. C., Arnold, J. A., et al. (2010). Global silicate mineralogy of the Moon from the Diviner Lunar Radiometer. *Science*, *329*(5998), 1507–1509. <https://doi.org/10.1126/science.1192196>
- Greenhagen, B. T., & Paige, D. A. (2006). Mapping lunar surface petrology using the mid-infrared emissivity maximum with the LRO Diviner Radiometer. In 37th annual lunar and planetary science conference (Vol. 37).
- Hamilton, V. E. (2000). Thermal infrared emission spectroscopy of the pyroxene mineral series. *Journal of Geophysical Research*, *105*, 9701–9716. <https://doi.org/10.1029/1999JE001112>
- Heiken, G. H., McKay, D. S., & Fruland, R. M. (1973). Apollo 16 soils: Grain size analyses and petrography. In Lunar and Planetary Science Conference Proceedings (Vol. 4, p. 251).
- Henderson, B. G., & Jakosky, B. M. (1994). Near-surface thermal gradients and their effects on mid-infrared emission spectra of planetary surfaces. *Journal of Geophysical Research*, *99*, 19,063–19,073. <https://doi.org/10.1029/94JE01861>
- Henderson, B. G., & Jakosky, B. M. (1997). Near-surface thermal gradients and mid-IR emission spectra: A new model including scattering and application to real data. *Journal of Geophysical Research*, *102*, 6567–6580. <https://doi.org/10.1029/96JE03781>
- Jackson, C. R. M., Cheek, L. C., Williams, K. B., Hanna, K. D., Pieters, C. M., Parman, S. W., et al. (2014). Visible-infrared spectral properties of iron-bearing aluminates spinel under lunar-like redox conditions. *American Mineralogist*, *99*(10), 1821–1833. <https://doi.org/10.2138/am-2014-4793>
- Jolliff, B. L., Wiseman, S. A., Lawrence, S. J., Tran, T. N., Robinson, M. S., Sato, H., et al. (2011). Compton-Belkovich: Nonmare silicic volcanism on the Moon's far side. *Nature Geoscience*, *4*(8), 566–571. <https://doi.org/10.1038/ngeo1212>
- King, E. A., Butler, J. C., & Carman, M. F. (1971). *The lunar regolith as sampled by Apollo 11 and Apollo 12: Grain size analyses, modal analyses, and origins of particles*, Proc., 2nd lunar science Conf. (Vol. 1, pp. 737–746). Cambridge, MA: MIT Press.
- King, E. A., Butler, J. C., & Carman, M. F. (1972a). Chondrules in Apollo 14 breccias and estimation of lunar surface exposure ages from grain size analyses. In Lunar and Planetary Science Conference (Vol. 3, p. 449).
- King Jr, E. A., Butler, J. C., & Carman, M. F. (1972b). Chondrules in Apollo 14 samples and size analyses of Apollo 14 and 15 fines. In Lunar and Planetary Science Conference Proceedings (Vol. 3, p. 673).
- Logan, L. M., & Hunt, G. R. (1970). Emission spectra of particulate silicates under simulated lunar conditions. *Journal of Geophysical Research*, *75*, 6539–6548. <https://doi.org/10.1029/JB075i032p06539>
- Logan, L. M., Hunt, G. R., Salisbury, J. W., & Balsamo, S. R. (1973). Compositional implications of Christiansen frequency maximums for infrared remote sensing applications. *Journal of Geophysical Research*, *78*, 4983–5003. <https://doi.org/10.1029/JB078i023p04983>
- Lucey, P. G., Greenhagen, B. T., Song, E., Arnold, J. A., Lemelin, M., Hanna, K. D., et al. (2017). Space weathering effects in Diviner Lunar Radiometer multispectral infrared measurements of the lunar Christiansen feature: Characteristics and mitigation. *Icarus*, *283*, 343–351. <https://doi.org/10.1016/j.icarus.2016.05.010>
- Lyon, R. J. P. (1964). Evaluation of infrared spectrophotometry for compositional analysis of lunar and planetary soils. Part II Rough and powdered surfaces, NASA Rep. CR-100, 264 pp.
- Marriner, C. M., Donaldson Hanna K. L., Bowles N. E., Greenhagen B. T., Jackson C. R. M., Cheek L., et al. (2015). Spectral characterisation of spinel-anorthite mixtures in the thermal infrared. In Lunar and Planetary Science Conference (Vol. 46, p. 1750).
- Marriner, C. M., Donaldson Hanna K. L., Bowles N. E., Prissel T. C., C. R. M. Jackson, Cheek L., et al. (2014) Characterisation of a terrestrial low-iron pink spinel as an analogue to support thermal infrared observations of the Moon. In Lunar and Planetary Science Conference, vol. 45, p. 1806.
- McKay, D. S., Fruland, R. M., & Heiken, G. H. (1974). Grain size and the evolution of lunar soils. In Lunar and Planetary Science Conference Proceedings (Vol. 5, pp. 887–906).
- McKay, D. S., Heiken, G. H., Taylor, R. M., Clanton, U. S., Morrison, D. A., & Ladle, G. H. (1972). Apollo 14 soils: Size distribution and particle types. In Lunar and Planetary Science Conference Proceedings (Vol. 3, p. 983).
- McKay, D. S., & Williams, R. J. (1979). A geologic assessment of potential lunar ores. In Space Resources and Space Settlements.
- Millán, L., Thomas, I., & Bowles, N. (2011). Lunar regolith thermal gradients and emission spectra: Modeling and validation.
- Mustard, J. F., & Hays, J. E. (1997). Effects of hyperfine particles on reflectance spectra from 0.3 to 25 μm . *Icarus*, *125*(1), 145–163.
- Nash, D. B., Salisbury, J. W., Conel, J. E., Lucey, P. G., & Christensen, P. R. (1993). Evaluation of infrared emission spectroscopy for mapping the Moon's surface composition from lunar orbit. *Journal of Geophysical Research*, *98*, 23,535–23,552. <https://doi.org/10.1029/93JE02604>
- Nekvasil, H., Lindsley, D. H., DiFrancesco, N., Catalano, T., Coraor, A. E., & Charlier, B. (2015). uncommon behavior of plagioclase and the ancient lunar crust. *Geophysical Research Letters*, *42*, 10,573–10,579. <https://doi.org/10.1002/2015GL066726>
- Paige, D. A., Foote, M. C., Greenhagen, B. T., Schofield, J. T., Calcutt, S., Vasavada, A. R., et al. (2010). The Lunar Reconnaissance Orbiter Diviner Lunar Radiometer Experiment. *Space Science Reviews*, *150*(1-4), 125–160. <https://doi.org/10.1007/s11214-009-9529-2>

- Paige, D. A., Siegler, M. A., Zhang, J. A., Hayne, P. O., Foote, E. J., Bennett, K. A., et al. (2010). Diviner Lunar Radiometer observations of cold traps in the Moon's south polar region. *Science*, *330*(6003), 479–482.
- Papike, J., Taylor, L., & Simon, S. (1991). Lunar minerals. In *Lunar sourcebook* (pp. 121–181). Cambridge, UK: Cambridge University Press.
- Papike, J. J., Hodges, F. N., Bence, A. E., Cameron, M., & Rhodes, J. M. (1976). Mare basalts: Crystal chemistry, mineralogy, and petrology. *Reviews of Geophysics*, *14*, 475–540. <https://doi.org/10.1029/RG014i004p00475>
- Papike, J. J., Ryder, G., & Shearer, C. K. (1998). Lunar samples. *Reviews in Mineralogy*, *36*, 1–189.
- Papike, J. J., Simon, S. B., & Laul, J. C. (1982). The lunar regolith: Chemistry, mineralogy, and petrology. *Reviews of Geophysics*, *20*, 761–826. <https://doi.org/10.1029/RG020i004p00761>
- Papike, J. J., & Vaniman, D. T. (1978). The lunar mare basalt suite. *Geophysical Research Letters*, *5*, 433–436. <https://doi.org/10.1029/GL005i006p00433>
- Pieters, C. M., Besse, S., Boardman, J., Buratti, B., Cheek, L., Clark, R. N., et al. (2011). Mg-spinel lithology: A new rock type on the lunar farside. *Journal of Geophysical Research*, *116*, E00G08. <https://doi.org/10.1029/2010JE003727>
- Pieters, C. M., Fischer, E. M., Rode, O., & Basu, A. (1993). Optical effects of space weathering: The role of the finest fraction. *Journal of Geophysical Research*, *98*, 20,817–20,824. <https://doi.org/10.1029/93JE02467>
- Pieters, C. M., Hanna, K. D., Cheek, L., Dhingra, D., Prissel, T., Jackson, C., et al. (2014). The distribution of Mg-spinel across the Moon and constraints on crustal origin. *American Mineralogist*, *99*(10), 1893–1910. <https://doi.org/10.2138/am-2014-4776>
- Ruff, S. W., Christensen, P. R., Barbera, P. W., & Anderson, D. L. (1997). Quantitative thermal emission spectroscopy of minerals: A laboratory technique for measurement and calibration. *Journal of Geophysical Research*, *102*, 14,899–14,913. <https://doi.org/10.1029/97JB00593>
- Rutherford, M. J., Dixon, S., & Hess, P. (1980). Ilmenite saturation at high pressure in KREEP basalts: Origin of KREEP and HI-TiO₂ in mare basalts, In 11th Lunar and Planetary Science Conference, Abstract 1344.
- Salisbury, J. W., & Eastes, J. W. (1985). The effect of particle size and porosity on spectral contrast in the mid-infrared. *Icarus*, *64*(3), 586–588. [https://doi.org/10.1016/0019-1035\(85\)90078-8](https://doi.org/10.1016/0019-1035(85)90078-8)
- Salisbury, J. W., Hapke, B., & Eastes, J. W. (1987). Usefulness of weak bands in midinfrared remote sensing of particulate planetary surfaces. *Journal of Geophysical Research*, *92*, 702–710. <https://doi.org/10.1029/JB092iB01p00702>
- Salisbury, J. W., Murcray, D. G., Williams, W. J., & Blatherwick, R. D. (1995). Thermal infrared spectra of the Moon. *Icarus*, *115*(1), 181–190. <https://doi.org/10.1006/icar.1995.1087>
- Salisbury, J. W., & Wald, A. (1992). The role of volume scattering in reducing spectral contrast of reststrahlen bands in spectra of powdered minerals. *Icarus*, *96*(1), 121–128. [https://doi.org/10.1016/0019-1035\(92\)90009-V](https://doi.org/10.1016/0019-1035(92)90009-V)
- Salisbury, J. W., Vincent, R. K., Logan, L. M., & Hunt, G. R. (1970). Infrared emissivity of lunar surface features: 2. Interpretation. *Journal of Geophysical Research*, *75*(14), 2671–2682.
- Shirley, K. A. (2018). The effects of particle size and albedo on mid-infrared spectroscopy for the Moon (doctoral dissertation). State University of New York at Stony Brook, ProQuest 10823197.
- Shirley, K. A., McDougall, D., & Glotch, T. D. (2018). The effect of albedo on mid-infrared spectra of airless bodies with implications for Diviner data analysis. In 49th Lunar and Planetary Science Conference, Abstract 1298.
- Siegler, M., Paige, D., Williams, J. P., & Bills, B. (2015). Evolution of lunar polar ice stability. *Icarus*, *255*, 78–87. <https://doi.org/10.1016/j.icarus.2014.09.037>
- Siegler, M. A., Miller, R. S., Keane, J. T., Laneuville, M., Paige, D. A., Matsuyama, I., et al. (2016). Lunar true polar wander inferred from polar hydrogen. *Nature*, *531*(7595), 480–484. <https://doi.org/10.1038/nature17166>
- Smith, J. V., & Steele, I. M. (1976). Lunar mineralogy: A heavenly detective story, Part II. *American Mineralogist*, *61*, 1059–1116.
- Song, E., Bandfield, J. L., Lucey, P. G., Greenhagen, B. T., & Paige, D. A. (2013). Bulk mineralogy of lunar crater central peaks via thermal infrared spectra from the Diviner Lunar Radiometer: A study of the Moon's crustal composition at depth. *Journal of Geophysical Research: Planets*, *118*, 689–707. <https://doi.org/10.1002/jgre.20065>
- Spitzer, W. G., & Kleinman, D. A. (1961). Infrared lattice bands of quartz. *Physical Review*, *121*(5), 1324–1335. <https://doi.org/10.1103/PhysRev.121.1324>
- Taylor, G. J. (2009). Ancient lunar crust: Origin, composition, and implications. *Elements*, *5*(1), 17–22. <https://doi.org/10.2113/gselements.5.1.17>
- Thomas, I. R., Greenhagen, B. T., Bowles, N. E., Donaldson Hanna, K. L., Temple, J., & Calcutt, S. B. (2012). A new experimental setup for making thermal emission measurements in a simulated lunar environment. *Review of Scientific Instruments*, *83*(12). <https://doi.org/10.1063/1.4769084>
- Vaniman, D. T., & Papike, J. J. (1980). Lunar highland melt rocks-chemistry, petrology and silicate mineralogy. In *Lunar Highlands Crust* (pp. 271–337).
- Vasavada, A. R., Bandfield, J. L., Greenhagen, B. T., Hayne, P. O., Siegler, M. A., Williams, J.-P., & Paige, D. A. (2012). Lunar equatorial surface temperatures and regolith properties from the Diviner Lunar Radiometer Experiment. *Journal of Geophysical Research*, *117*, E00H18. <https://doi.org/10.1029/2011JE003987>
- Vincent, R. K., & Hunt, G. R. (1968). Infrared reflectance from mat surfaces. *Applied Optics*, *7*(1), 53–59.
- Wieczorek, M. A., Jolliff, B. L., Khan, A., Pritchard, M. E., Weiss, B. P., Williams, J. D., et al. (2006). New views of the moon. *Reviews in Mineralogy and Geochemistry*, *60*(1), 221–364. <https://doi.org/10.2138/rmg.2006.60.3>
- Williams, J. P., Paige, D. A., Greenhagen, B. T., & Sefton-Nash, E. (2017). The global surface temperatures of the Moon as measured by the Diviner Lunar Radiometer Experiment. *Icarus*, *283*, 300–325. <https://doi.org/10.1016/j.icarus.2016.08.012>
- Williams, K. B., Jackson, C. R. M., Cheek, L. C., Donaldson-Hanna, K. L., Parman, S. W., Pieters, C. M., et al. (2016). Reflectance spectroscopy of chromium-bearing spinel with application to recent orbital data from the Moon. *American Mineralogist*, *101*(3), 726–734. <https://doi.org/10.2138/am-2016-5535>